Land Surface Modeling in the Himalayas: On the Importance of Evaporative Fluxes for the Water Balance of a High-Elevation Catchment

Pascal Buri[1] , Simone Fatichi[2] , Thomas E. Shaw[1] , Evan S. Miles[1] , Michael J. McCarthy[1] , Catriona L. Fyffe[3,4] , Stefan Fugger[1,5] , Shaoting Ren[1,6] , Marin Kneib[1,5] , Achille Jouberton[1,5] , Jakob Steiner[7,8] , Koji Fujita[9] , and Francesca Pellicciotti[1,4]

[1]Swiss Federal Institute for Forest, Snow, and Landscape Research WSL, Birmensdorf, Switzerland, [2]Department of Civil and Environmental Engineering, National University of Singapore, Singapore, Singapore, [3]Department of Geography and Environmental Sciences, Northumbria University, Newcastle upon Tyne, UK, [4]Institute of Science and Technology Austria (ISTA), Klosterneuburg, Austria, [5]Institute of Environmental Engineering, ETH Zürich, Zürich, Switzerland, [6]State Key Laboratory of Tibetan Plateau Earth System, Environment and Resources (TPESER), Institute of Tibetan Plateau Research, Chinese Academy of Sciences, Beijing, China, [7]International Centre for Integrated Mountain Development, Kathmandu, Nepal, [8]Institute of Geography and Regional Science, University of Graz, Graz, Austria, [9]Graduate School of Environmental Studies, Nagoya University, Nagoya, Japan

Abstract High Mountain Asia (HMA) is among the most vulnerable water towers globally and yet future projections of water availability in and from its high-mountain catchments remain uncertain, as their hydrologic response to ongoing environmental changes is complex. Mechanistic modeling approaches incorporating cryospheric, hydrological, and vegetation processes in high spatial, temporal, and physical detail have never been applied for high-elevation catchments of HMA. We use a land surface model at high spatial and temporal resolution (100 m and hourly) to simulate the coupled dynamics of energy, water, and vegetation for the 350 km² Langtang catchment (Nepal). We compare our model outputs for one hydrological year against a large set of observations to gain insight into the partitioning of the water balance at the subseasonal scale and across elevation bands. During the simulated hydrological year, we find that evapotranspiration is a key component of the total water balance, as it causes about the equivalent of 20% of all the available precipitation or 154% of the water production from glacier melt in the basin to return directly to the atmosphere. The depletion of the cryospheric water budget is dominated by snow melt, but at high elevations is primarily dictated by snow and ice sublimation. Snow sublimation is the dominant vapor flux (49%) at the catchment scale, accounting for the equivalent of 11% of snowfall, 17% of snowmelt, and 75% of ice melt, respectively. We conclude that simulations should consider sublimation and other evaporative fluxes explicitly, as otherwise water balance estimates can be ill-quantified.

Plain Language Summary The Himalayan mountains are a crucial source of water for local communities and the densely populated lowlands. Snow and glaciers are important for the water cycle in mountains, and many studies have focused on them. However, vegetation can play a central role, too. To better understand the water cycle in a high-elevation Himalayan basin, we use a computer model that considers physical processes of snow and glaciers, soil, and vegetation in high detail. We simulate the catchment water balance and investigate the importance of single components at different elevations and in different seasons. We find that the transfer of water, in vapor form from the ground, snow and ice and the transpiration of plants are important for the water budget in the study basin, causing more water to return to the atmosphere than ice melt contributing to river runoff. Above 6,500 m above sea level, it is the transformation of snow into water vapor and below 4,000 m the transpiration from vegetation that dominate the water budget. We conclude that models simulating the water cycle in high mountain regions should consider vapor fluxes, as otherwise estimates of the water balance can be misleading.

1. Introduction

High Mountain Asia (HMA) contains the largest ice mass outside the polar ice sheets (RGI Consortium, 2017). It is among the most important and yet most vulnerable mountain water towers, i.e., high-elevation regions which provide freshwater for downstream regions (Bandyopadhyay et al., 1997; Immerzeel et al., 2020; Viviroli

et al., 2007). The accelerated transformation of snow (e.g., Lau et al., 2010; Usha et al., 2022) and ice (e.g., Brun et al., 2017; Hugonnet et al., 2021; Maurer et al., 2019; Shean et al., 2020) into melt water destabilizes freshwater supply rates with large socio-economic effects for high mountain communities (McDowell et al., 2022) and downstream populations (Azam et al., 2021; Biemans et al., 2019; Pritchard, 2019; Yao et al., 2022). Ongoing changes in precipitation, permafrost thaw, subsurface water storage, and evapotranspiration implied by climate change, further complicate the hydrologic response of high-mountain catchments as they alter surface runoff and modify water supply to mountain and lowland areas (Yao et al., 2022). This contributes to large uncertainties in future projections of water availability within and from mountain regions: although glacier runoff is expected to peak, especially in the Indus and Ganges basins, in the next few decades under most climate change scenarios (Huss & Hock, 2018; Nie et al., 2021), the impact on downstream water supply remains unclear, and a considerable portion might be lost through evapotranspiration and atmospherically recycled.

Numerous hydrological studies have been conducted in HMA at the scale of the entire Himalayan arc (e.g., Immerzeel et al., 2010; Lutz et al., 2014), for distinct regions (e.g., Khadka et al., 2020; Pohl et al., 2017) or individual catchments (e.g., Duethmann et al., 2016; Fujita & Sakai, 2014; Immerzeel et al., 2013; Jouberton et al., 2022; Mimeau et al., 2019; Pohl et al., 2015; Ragettli et al., 2015, Ragettli, Immerzeel, et al., 2016) to investigate the hydrology of glacierized mountainous areas. However, all of these efforts to simulate HMA's glacierized catchment hydrology rely on spatial, temporal, and process-related simplifications, partly dictated by a lack of ground data that have steered modeling choices toward conceptual approaches. While a high degree of simplification can be helpful for computationally efficient, long-term simulations into the past or for future projections, simplifications in the spatial representation (e.g., hydrological units versus gridded representation), spatiotemporal resolution (coarse versus fine-scale) and processes (e.g., empirical versus physics-based) can obscure potentially relevant mechanisms and hinder comparisons of individual processes or water balance components (Mastrotheodoros et al., 2019; van Tiel et al., 2020).

Mechanistic modeling approaches that represent all processes of the land-surface interaction have not been applied for high-elevation catchments of HMA yet. Land surface models incorporate cryospheric, hydrological, and vegetation processes in high spatial, temporal, and physical detail for diverse land surfaces and enable a mechanistic understanding of the functioning of distinct hydrological components of high-elevation catchments. Explicit simulations of the energy and mass budgets provide estimates of vapor fluxes, which are assumed to be nonnegligible in the water budget of glacierized HMA basins but are rarely quantified (e.g., Azam et al., 2021). In conceptual models, catchment-scale evapotranspiration is often derived as a residual of the bulk water balance or parameterized with empirical equations (e.g., Priestley–Taylor equation in Ragettli et al. (2015); Hamon equation in Sorg et al. (2014)) that do not account for vegetation dynamics or soil-vegetation interactions. Snow sublimation remains, despite decades of research and the agreement on its nonnegligible role in the alpine water balance (Broxton et al., 2015; MacDonald et al., 2010; Strasser et al., 2008), difficult to convincingly quantify. In HMA, snow sublimation has never been simulated at the catchment scale, and its quantities remain elusive. Remote sensing (e.g., Martens et al., 2017) and reanalysis products (e.g., Lu et al., 2021; Muñoz-Sabater, 2019) that provide continuous (e.g., daily) time series of modeled evapotranspiration for all land surface types are only available at coarse spatial resolution (>~10 km) and therefore not suitable to account for the supposedly high spatiotemporal variability of latent heat fluxes in mountainous terrain in a reliable way.

As a result, the importance of evapotranspiration for the hydrology of high altitude environments remains unknown and the rare existing estimates of snow sublimation (Gascoin, 2021; Mandal et al., 2022; Reba et al., 2012; Stigter et al., 2018) refer only to the point or regional scale.

In this study we use a distributed, physically based mechanistic land surface model that simulates the coupled dynamics of energy, water, and vegetation at the land surface for a 350 km^2 Himalayan catchment and explicitly calculates energy and mass fluxes with very high resolution in space and time (100 m and hourly). The meteorological forcing is based on a dense network of multiyear, in situ station data. With the land surface model, we simulate the energy and mass fluxes of the catchment for one data rich hydrological year and compare model outputs against a variety of independent, multisource observational data. Our aim is to enhance the understanding of the hydrologic functioning of a high-elevation glacierized catchment that is based on a model at the frontiers of current research on land-surface interactions in complex terrains. Specifically, we shed light on the nontrivial role of vapor fluxes (i.e., evaporation, sublimation, transpiration) in the water budget of such an extreme environment. We will do this by (a) quantifying the importance of individual water balance components and how they vary
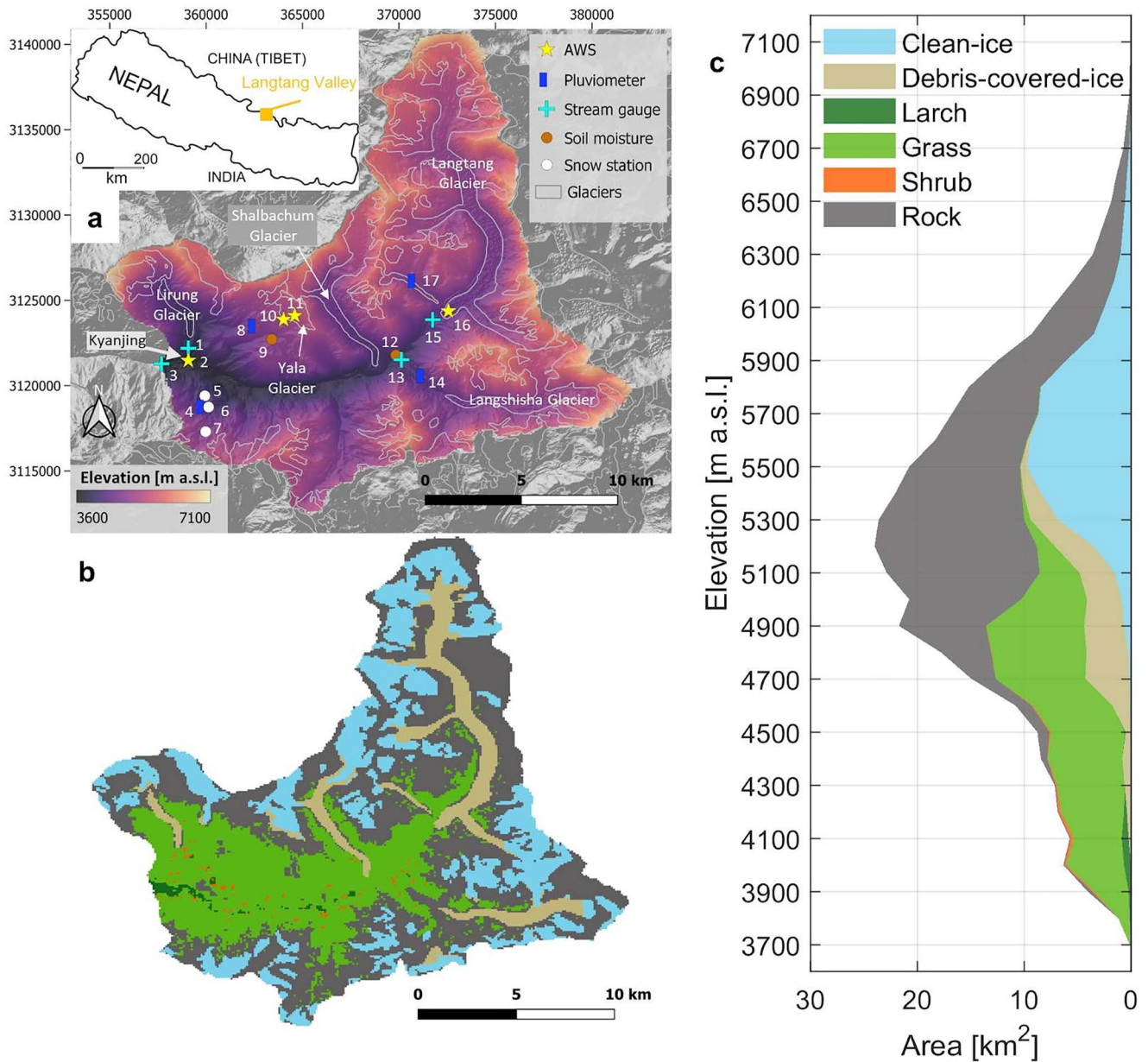
Figure 1. The upper Langtang Valley catchment in the central Nepalese Himalayas (inset map): (a) map of observational stations running over the period of interest, with the main automatic weather station (AWS) in Kyanjing (AWS$_{KYA}$; number 2, see Table S1 in Supporting Information S1 for details); (b) spatial distribution of land cover; (c) vertical distribution (hypsometry) of land cover within the catchment.

seasonally and with elevation and (b) identifying the key physical processes driving the changes in the water balance.

2. Study Site and Climate

The study area is the upper Langtang Valley catchment (350 km^2 surface area), a high-elevation (3,650–7,227 m.a.s.l.) basin in the central Nepalese Himalayas (Figure 1). Its principal river, Langtang Khola, drains into the Trisuli River and eventually contributes to the Ganges River. Numerous research campaigns have been conducted in the valley since the 1980's, with a strong focus on its meteorology (e.g., Bonekamp et al., 2018; Collier & Immerzeel, 2015; Fujita et al., 1997; Heynen et al., 2016; Immerzeel et al., 2014; Morinaga et al., 1987; Seko, 1987; Seko & Takahashi, 1991; Steiner, Gurung, et al., 2021; Ueno & Yamada, 1990; Ueno et al., 1993),

glaciology (e.g., Fujita et al., 1998; Higuchi, 1984; Pellicciotti et al., 2015; Ragettli, Bolch, et al., 2016; Steiner, Kraaijenbrink, et al., 2021; Wijngaard et al., 2019) and glacio-hydrology (e.g., Braun et al., 1993; Immerzeel, Van Beek, et al., 2012; Konz et al., 2007; Racoviteanu et al., 2013; Ragettli et al., 2015; Ragettli, Immerzeel, et al., 2016; Wilson et al., 2016).

The upper Langtang Valley is highly glacierized (31%) and one-third of its glacier area is debris-covered (Figure 1). About 26% of the basin is vegetated, comprising grassland (96%) and marginal zones of shrubs and larch (4%). Rocky surfaces comprise 43% of the catchment, particularly in high-elevation and/or steep slopes where no soil or glacier ice can form.

The climatic conditions in the catchment are mainly driven by the South Asian monsoon, affected by dominant easterly winds in summer and westerly winds in winter (Immerzeel, Van Beek, et al., 2012). Most of the annual precipitation (>75%) falls in the monsoon season between mid-June and September (Shaw et al., 2022; Uppala et al., 2005). Precipitation is assumed to increase with elevation both in monsoon and dry (winter) seasons (Seko, 1987). Concomitant with the high precipitation rates, the monsoon period brings warmer and cloudier conditions (e.g., Ragettli et al., 2015), and the highest rates of glacier ablation occur during summer, which categorizes glaciers in this region into summer-accumulation type glaciers (e.g., Ageta & Higuchi, 1984; Fujita, 2008).

3. Methods and Data

3.1. The Land Surface Model Tethys and Chloris

Model simulations were performed using the distributed, mechanistic land surface model *Tethys & Chloris* (*T&C*; Fatichi et al., 2012a, 2012b). *T&C* simulates the coupled dynamics of energy, water (both at the hourly scale), and vegetation dynamics (carbon and nutrient cycles at the daily scale) accounting for plant biophysical and physiological properties. It represents bare soil, rock, vegetated, water, snow-covered, ice, and debris-covered ground/glacier surfaces per grid cell (100-m spatial resolution in this study).

T&C generally assumes, for each grid cell, a single value of prognostic surface temperature, T_s, which represents the homogeneous radiative temperature of the surface in a given computational element. When snow cover is present at the ground and (if in a vegetated element) the vegetation is snow free, the model computes two prognostic temperatures, T_s (snowpack radiative temperature) and T_{veg} (temperature of snow-free vegetated surfaces). The prognostic surface temperature is the central variable for the estimation of energy fluxes as it is used to close the energy balance. All energy fluxes, net radiation, sensible heat, latent heat, ground heat, and incoming heat with precipitation, are calculated based on T_s.

In order to estimate the transfer of heat, water vapor (i.e., sensible and latent heat fluxes) and CO_2 between the land surface and the reference height, *T&C* employs a resistance analogy scheme (Brutsaert, 2005; Garratt, 1992) by separately calculating aerodynamic, undercanopy, leaf boundary layer, soil, stomatal (for sunlit and shaded leaves), and soil-to-root resistances. The aerodynamic resistance is based on a simplified Monin-Obukhov solution using a bulk transfer coefficient (Mascart et al., 1995) with aerodynamic, thermal, and vapor roughness lengths calculated based on Brutsaert (1982).

In *T&C*, the dynamics of each grid cell are resolved using hourly meteorological forcing, considering local shading cast by far-field terrain, and boundary conditions for soil and vegetation properties (Fatichi et al., 2012a). Spatial interactions are introduced by considering surface and subsurface water transfer among cells, vertically and laterally (e.g., Hopp et al., 2016). Therefore, a quasi-3D representation of land surface dynamics is achieved, where incoming energy and lateral water transfers can influence the variability of the simulated fluxes and states in a given cell (Fatichi et al., 2012a).

T&C has been applied to a large spectrum of ecosystems (e.g., grassland, forest, desert, shrubland, cropland), environmental conditions (e.g., subarctic, high-alpine, Mediterranean, continental, tropical), and scales (from entire mountain ranges to the catchment and plot (few hundreds of meters) scale; e.g., Botter et al., 2021; Fatichi et al., 2021; Fugger et al., 2022; Fyffe et al., 2021; Mastrotheodoros et al., 2020; Paschalis et al., 2018; Shaw et al., 2022). Given its mechanistic nature, the model requires minimal calibration (Fatichi et al., 2016), and does not rely on calibration with aggregated variables such as catchment runoff, which represent the integrated response of a catchment and not individual processes. It has instead physical parameters (e.g., soil hydraulic properties, supraglacial debris properties) that can be estimated from observations, expert knowledge or

values from the literature. A selection of model parameters can be found in Text S3 and Table S3 in Supporting Information S1.

3.1.1. The Cryosphere

The melt and accumulation of glacier ice and snow, and the ice melt under debris are explicitly simulated in *T&C* (Fugger et al., 2022). Snowpack and icepack dynamics are accounted for by solving the energy balance. Snow can be intercepted by the vegetation or it falls to the ground, where it accumulates and successively melts. Sublimation is computed as the flux of water vapor from a frozen surface considering the snowpack temperature and the latent heat of sublimation (Pomeroy et al., 1998). The snowpack and ice column are each represented as a single layer with conduction of energy down to a depth of 2 m, below which snow or ice are assumed to be isothermal (Fugger et al., 2022). Snow has a water content which can refreeze, whereas melted water in the ice pack is evacuated through runoff without refreezing. Transient debris temperature profiles are computed with the heat diffusion equation using iterative numerical methods (e.g., Reid & Brock, 2010). The conductive energy flux at the base of the debris is used for ice melt (Fugger et al., 2022).

Gravitational snow redistribution is simulated and routed based on the local terrain and snow depth for each time step, following a simple avalanche routine (Bernhardt & Schulz, 2010).

Precipitation is partitioned into rain, snow, and mixed (sleet) phases, using the wet-bulb temperature, instead of air temperature, as the main predictor for precipitation phase (Ding et al., 2014). The snow albedo scheme implemented into *T&C* takes into account fresh snow falls, snow aging, sleet albedo, cloud cover, and sun angle (Ding et al., 2017). Details of the *T&C* energy balance model over snow, ice, and debris-cover ice are described in detail in Fyffe et al. (2021) and Fugger et al. (2022).

3.1.2. The Pedosphere

We used the Saxton and Rawls (2006) pedotransfer function to compute soil hydraulic parameters. The soil hydrology module in *T&C* solves the 1-D Richard's equation in the vertical direction and uses a heat diffusion solution (Núñez et al., 2010) to compute the soil temperature profile (Botter et al., 2021). The solution accounts for phase changes, soil freezing, and thawing, with latent energy being constrained by the availability of water. The soil is discretized into *n* layers of varying thickness, which can individually, based on local topography, laterally transfer water, following the kinematic wave approximation (e.g., Hopp et al., 2016). Saturated and unsaturated parts of the soil column are explicitly identified. Surface overland and channel flow are also solved through the kinematic equation. Runoff generation is made possible via saturation excess and infiltration excess mechanisms and depends on lateral moisture fluxes in the unsaturated and saturated zones as well as in runon of overland flow.

In *T&C*, the lowermost layer of the soil column is drained through the bottom resulting in a percolation flux from the soil column to the bedrock (soil-bedrock leakage) when the last layer of soil is saturated. This vertical subsurface flow provides a recharge to deep aquifers, representing a reservoir with a relatively long residence time that can be conceptualized as a lumped component at the watershed scale (Fatichi et al., 2012a).

3.1.3. The Biosphere

The vegetation module computes plant physiological processes including photosynthesis, respiration, vegetation phenology, carbon allocation to different plant compartments, and tissue turnover (Botter et al., 2021). Four different phenological states, relevant for leaf area index (LAI) dynamics and associated processes, e.g., for interception, are simulated and also affect plant carbon allocation (Arora & Boer, 2005): dormancy, maximum growth, normal growth, and senescence (Fatichi et al., 2012a). Root zone temperature, soil moisture, and photoperiod are used to control the beginning of the growing season (Mastrotheodoros et al., 2019).

3.2. Model Input Data

3.2.1. Topography

We used the ALOS World 3D-30 digital elevation model (DEM) derived from ALOS PRISM stereo images (spatial resolution of 30 m; Takaku et al., 2014), resampled to 100-m spatial resolution (nearest neighbor method) and with topographic sinks filled. The stream networks were derived from the filled DEM, with the outlet

defined as the runoff station at Kyanjing village (28.2091°N, 85.5475°E, 3,648 m.a.s.l.; indicated as station "3" in Figure 1a).

3.2.2. Glacier and Debris Maps

Glacierized area and initial ice volume were extracted from the glacier outlines of RGI 6.0 (RGI Consortium, 2017; gray outlines in Figure 1a) and the consensus glacier thickness estimates (Farinotti et al., 2019). Debris-covered glacier area (beige color in Figure 1b) was determined using outlines by Scherler et al. (2018). Debris thickness (Figure S2 in Supporting Information S1) was derived empirically as a function of velocity (Text S1.3 in Supporting Information S1). This approach was taken based on the observation that debris thickness patterns are often controlled by surface velocity, and that the relationship between the two variables has an inverse form (Anderson & Anderson, 2018; Kneib et al., 2023). At both Langtang and Lirung Glacier, the approach reproduces in situ observations (McCarthy et al., 2017, 2022) relatively well (Figures S24a and S24b in Supporting Information S1), and for all glaciers in the catchment, it reproduces expected debris thickness patterns, i.e., thicker debris down-glacier and toward the margins, and thinner debris up-glacier and toward the center line (Figures S2 and S24c in Supporting Information S1).

3.2.3. Land Cover and Soil Maps

We aggregated the vegetated area from the 2019 land cover product from PROBA-V satellite imagery (100 m spatial resolution; Buchhorn et al., 2020; Text S1.1 in Supporting Information S1) to forest, shrubs, and grassland and defined the three main plant functional types as larch (deciduous), shrub (deciduous), and grass (C3) based on specific botanical investigations (Beug & Miehe, 1999) and our own observations in the valley (Figures S4–S6 in Supporting Information S1). However, these are generalizations and in reality subpixel heterogeneities are likely. The vegetated area covers 26% (of which grass covers 96%, larch 2%, and shrubs 2%). The bare rock surface makes up 43% of the watershed area.

Soil textural properties (fractions of soil and clay, organic carbon content) were extracted from the SoilGrids 2.0 product (250-m spatial resolution; Poggio et al., 2021) as input in *T&C*. As a proxy for potential soil depths, we used surface slope (e.g., Ragettli et al., 2015). We assumed a maximum soil depth in our high-alpine watershed of 1 m for a flat surface (0° slope) and linearly reduced the soil depth with increasing slopes to a minimum of 0.01 m for slopes ≥60° (Figures S2 and S26 in Supporting Information S1). We defined 10 vertical soil layers for each soil pixel, with layer thicknesses increasing between 0.01 near the surface to 0.3 m (Table S3 in Supporting Information S1) and specified a quasi-impermeable layer at the assumed soil depth (closest layer).

3.2.4. Meteorological Forcing

T&C uses hourly air temperature, relative humidity, wind speed, precipitation, atmospheric pressure, incoming shortwave radiation (Text S1.4.1 in Supporting Information S1), and cloud cover fraction as meteorological inputs, which were derived from the automatic weather station (AWS) at Kyanjing (AWS$_{KYA}$; 28.21081°N, 85.56169°E, 3,862 m.a.s.l.; Figures 1 and S4 in Supporting Information S1; data from ICIMOD (2016a)). The meteorological record used in this study spans two hydrological years (1 October 2017–30 September 2019).

Data gaps at AWS$_{KYA}$ due to sensor failures (Table S2 and Text S1.4.2 in Supporting Information S1) were filled with data from AWS Yala Base Camp (AWS$_{YBC}$; 28.23252°N, 85.61208°E, 5,090 m.a.s.l.; Figure 1; data from ICIMOD (2016b)). Shortwave radiation instead was directly taken from ERA5-Land (Text S1.4.2 in Supporting Information S1) for the entire modeled period.

Measured precipitation at AWS$_{KYA}$ was spatially distributed based on seasonally variable vertical precipitation gradients derived from pluviometer data recorded at different locations and elevations in the upper Langtang Valley (Immerzeel et al., 2014). Large-scale studies have shown linear precipitation increases with elevation over mountain areas (e.g., Daly et al., 1994). But due to the lack of high-elevation observations, the validity of a continued linear vertical gradient is uncertain and a "plateau"-effect, i.e., constant or decreasing precipitation above a threshold elevation, has been suggested for different regions and at different scales in HMA (Immerzeel, Pellicciotti, et al., 2012). We determined a plateau at an elevation of 6,500 m.a.s.l. (with no increase in precipitation above) based upon a preliminary calibration exercise comparing simulated with altitudinally resolved glacier mass balance at the catchment scale. We tested three different maximum elevations (5,500, 6,000, and 6,500 m.a.s.l.), whereas the latter led to the best agreement with the independent glacier mass balance estimates based on E. Miles et al. (2021). Forcing the model with the two lower plateau elevations (5,500 and 6,000 m.a.s.l.)

resulted in an overestimation in glacier mass loss below 6,000 m.a.s.l. and accumulation deficit at higher elevations compared to the reference estimate. Further, we applied a vertical lapse rate for air temperature measured at AWS_{KYA} for each hour of the day and each month, derived from the regression of all available temperature measurements located in the study catchment for the period 2012–2019 (Heynen et al., 2016; Shaw et al., 2022; Steiner, Gurung, et al., 2021; Text S1.4.3 in Supporting Information S1). The lapsed air temperature over clean-ice glacier areas was reduced by a constant value of 1°C to account for the assumed katabatic cooling effect on the near surface boundary layer (Shaw et al., 2021; Shea & Moore, 2010; Text S1.4.3 in Supporting Information S1).

Cloud cover fraction, relative humidity, and wind speed were assumed to be spatially uniform for the entire catchment per time step, and only a constant vertical gradient was applied to direct shortwave radiation to account for the relative thinning of the atmosphere with increasing elevation (Marty et al., 2002; Text S1.4.3 in Supporting Information S1). Although, in reality, the spatial variability of these variables is assumed to be relatively high, only a much denser network of permanent observations capturing the orographic and synoptic atmospheric dynamics in the entire domain would allow their meaningful distribution in space.

3.2.5. Initial Conditions and Simulation Setup

The model study period is the hydrological year 2018/2019 (1 October 2018–30 September 2019), referred to as "2019" hereafter. To initialize *T&C*, we applied a 2-year model spin-up time prior to the target period, allowing the environmental variables, primarily vegetation (carbon pools), soil, and snow (water content), to adapt to the actual climatic conditions at different elevations and decouple from the initial conditions. However, many processes require a shorter spin-up period (days to weeks) and therefore the model output variables evaluated in the section below are partly also shown for the year prior to the target hydrological year 2019. The 2 years spin-up period here can therefore be seen as an upper bound time until which the entire hydrologic system is expected to be equilibrated. Due to major data gaps at AWS_{KYA} in the premonsoon and monsoon seasons 2017, the model spin-up time consists of an array of two identical meteorological forcings (two times the period 1 October 2017–30 September 2018).

From the initial hourly scale distributed simulations, we stored monthly, spatially distributed model outputs, hourly records at the locations of each station as well as spatially averaged hourly records for the entire watershed, per land cover type, and plant functional type.

The model's hourly temporal resolution is essential to account for processes with high diurnal variability (e.g., snow and ice melt and associated surface fluxes such as radiation and sensible heat) that considerably shape the runoff hydrograph.

4. Results

4.1. Model Evaluation

Langtang Valley is a unique monitoring site in HMA (Steiner, Gurung, et al., 2021), and this allowed comparison of model simulations with a variety of hydrometeorological and soil observations (Figure 2) at the plot scale. However, a mismatch in scales persists in all these evaluations, as we compare values measured at a specific point and simulated for a grid cell of 100 × 100 m, respectively. Additionally, all measurements are concentrated in the lower altitudes (maximum station elevation is 5,330 m.a.s.l., while the highest point in the catchment is 7,225 m.a.s.l.). Therefore, we also leverage remote sensing products to validate the model outputs across elevational bands and for different land cover classes (Figure 3). Additional model comparisons, aside from those in the main text, are in Supporting Information S1 (Figures S10–S19).

4.1.1. Plot-Scale Evaluation

4.1.1.1. Surface Temperature

Modeled surface temperature (T_s) refers to the skin temperature at the interface between the ground and the atmosphere. Surface temperature was not measured directly at most stations but could be inferred from the observed outgoing (upward) longwave radiation (assuming a constant emissivity value of 0.97 for all surfaces). *T&C* replicated the seasonal cycle and subseasonal fluctuations of measured surface temperatures well at AWS_{KYA} (grass surface) and AWS_{YBC} (bare soil) with a coefficient of determination (R^2) > 0.67 and a root mean square error (RMSE) < 4°C (Figure 2a). Strong but temporally limited deviations between observed and modeled values were apparent at stations with a transient snow cover (e.g., in September 2018 at AWS_{YBC}; Figure 2a), where the model
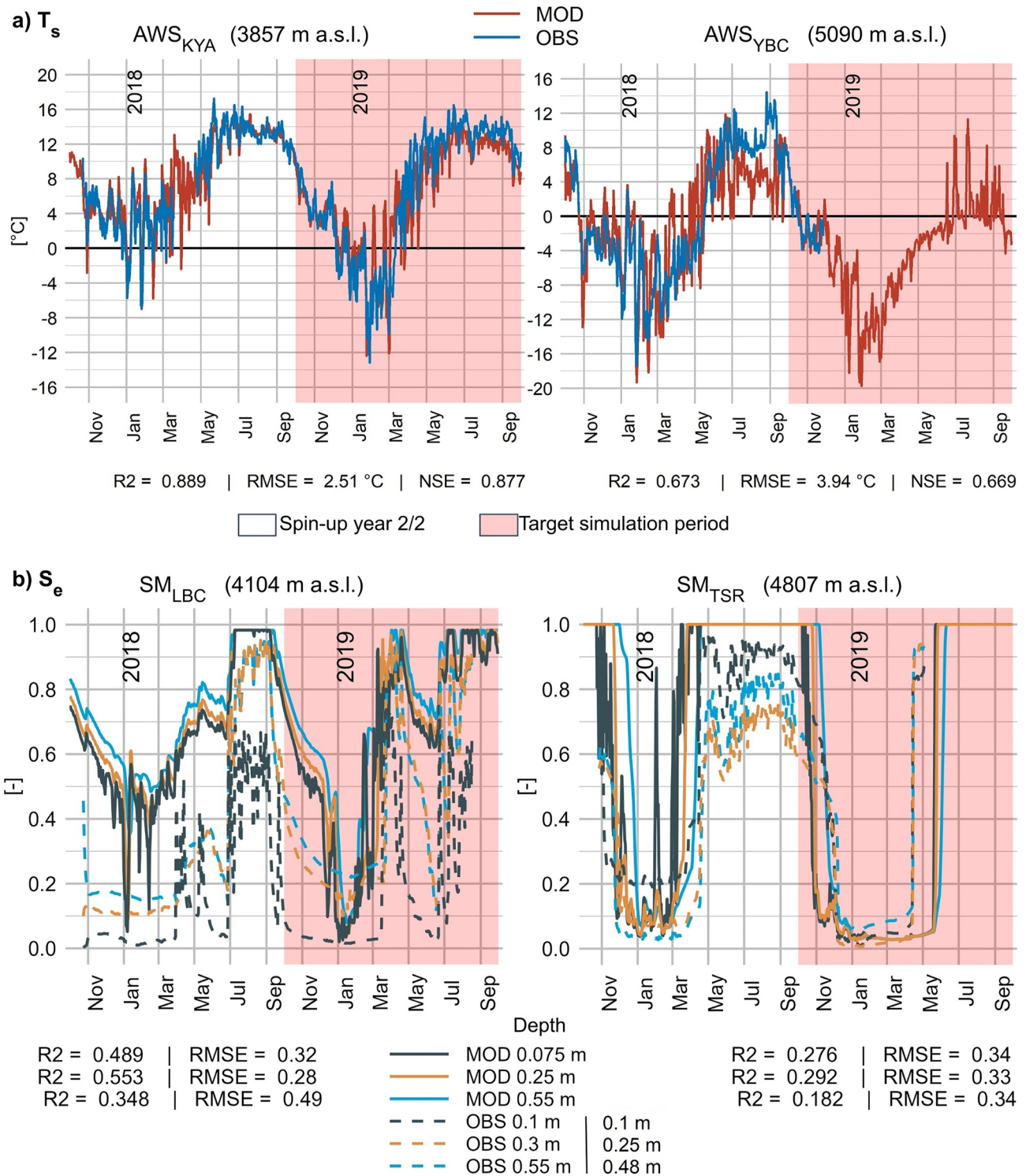
Figure 2. Comparison of observed and modeled variables at the point scale. (a) Daily mean surface temperature (T_s) as modeled and measured at AWSs Kyanjing (AWS$_{KYA}$) and Yala-BC (AWS$_{YBC}$) (observed values were derived from longwave radiation measurements). (b) Daily mean effective saturation (S_e) at different soil depths as modeled and measured at stations Langshisha-BC (SM$_{LBC}$) and Tserko Ri (SM$_{TSR}$). The red shading indicates the target simulation period (October 2018 until September 2019).

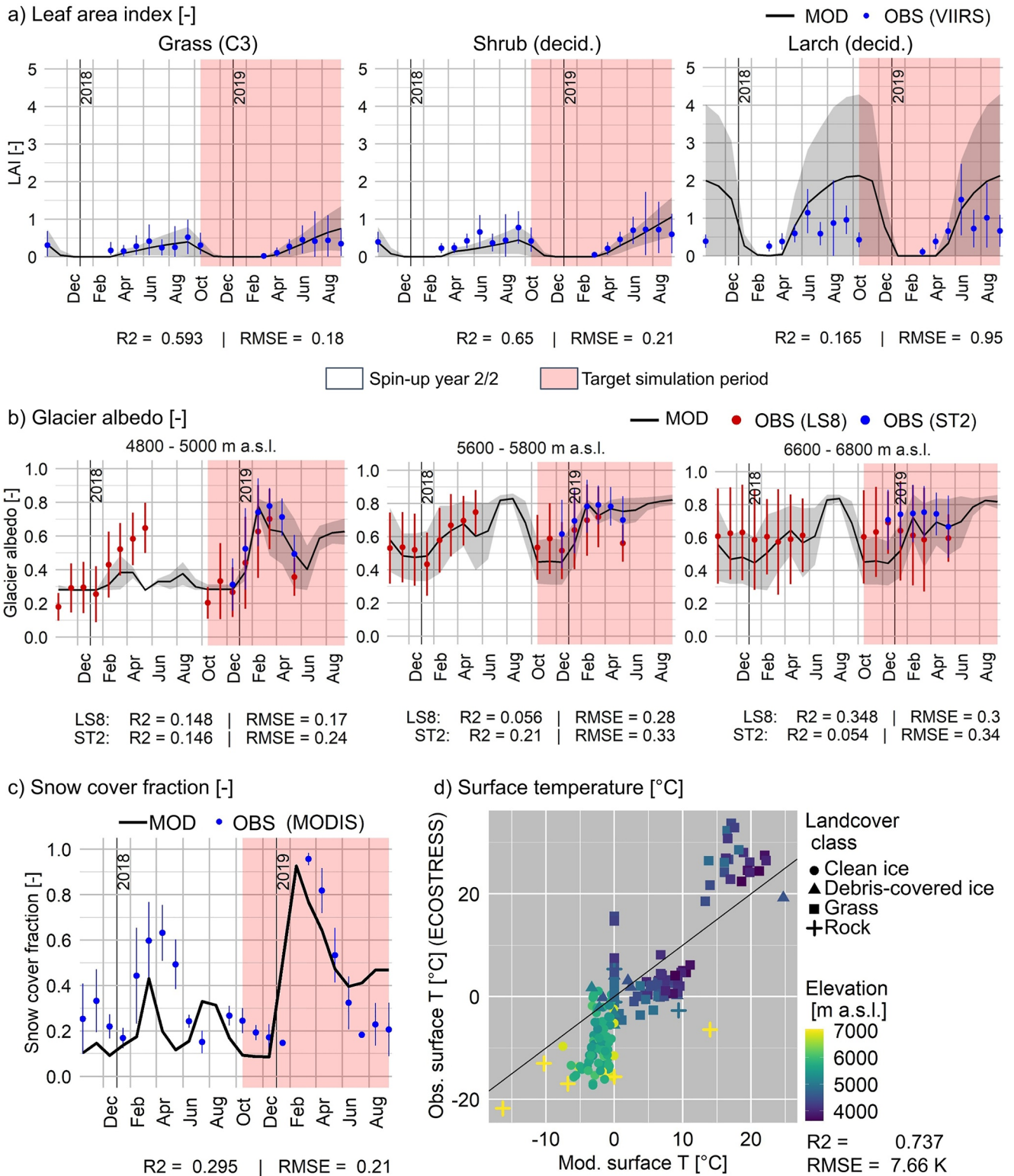**Figure 3.**

did not reproduce the nearby observed (solid) precipitation amounts (Figure S14 in Supporting Information S1; snow depth at AWS_{YBC} was not recorded).

4.1.1.2. Soil Moisture

Soil moisture was measured at two sites with three sensors within the soil column at each site. These measurements are only representative of the exact point location, since the soil properties, such as soil density, pore size distribution, organic content, soil depth, and preferential drainage paths, are highly variable in space (Schmitz & Sourell, 2000; Warrick & Nielsen, 1980). The modeled soil moisture, on the other hand, is representative for a soil profile of spatially averaged soil properties over a grid cell (Table S4 in Supporting Information S1), and therefore an integrated variable of subsurface hydrological dynamics. To normalize for this heterogeneity, we compare soil effective saturation (S_e, Figure 2b), which is a normalized metric of soil moisture and less dependent on the exact soil properties. S_e [−] of a soil layer i is defined as

$$S_e = \frac{\theta_i - \theta_{hy}}{\theta_{sat} - \theta_{hy}} \tag{1}$$

where θ_i is the liquid volumetric soil water content, θ_{hy} is the hygroscopic (residual) water content (imposing a water potential equal to −10,000 kPa) and θ_{sat} is the saturated water content, respectively (all dimensionless).

The model captures the intraannual cycle of S_e at both sites and reproduces the observed vertical water content structure, with more moisture deeper in the soil at the lower fieldsite (Langshisha-BC, SM_{LBC}) and more water close to the surface in the higher site (Tserko Ri, SM_{TSR}). Both profiles show low S_e in winter and premonsoon and peak saturation during the monsoon season. This seasonal pattern is more pronounced at the higher SM_{TSR} site, where the modeled saturation also agrees well throughout the two hydrological years shown here. At the SM_{LBC} site, the model tends to overestimate S_e, but preserving the annual cycle. At SM_{TSR}, it is the summer period which the model slightly overestimates, whereas the winter season and transition to/from it is replicated well. An overestimation in soil moisture might lead to increased runoff contribution and higher evapotranspiration in some areas.

4.1.2. Distributed-Scale Evaluation

4.1.2.1. Leaf Area Index

We averaged simulated monthly mean LAIs over all grid cells vegetated with grass, shrub and larch, respectively, and compared it to the averaged satellite-derived LAIs (VIIRS; Text S4.2 in Supporting Information S1) of the same cells (Figure 3a). The seasonality of LAI (high in summer, low in winter) was captured by the model, with R^2 (based on monthly averages over the target year) between 0.165 (larch) and 0.651 (shrub), and RMSE between 0.18 (grass) and 0.95 (larch; Figure 3a). The mismatch between simulated and observed LAIs during the monsoon season is likely due to a bias in the observations related to the high uncertainty due to cloud cover and complex topographies in general. Larches cover only a very small part of the catchment (0.56%, i.e., <2 km^2), and by relying on LAI from VIIRS (500 m spatial resolution) subpixel errors, i.e., mixing e.g., with grass, but also betula, fir, juniper, and rhododendron, which were not represented in our land cover product, but observed in the catchment, are therefore very likely. Although also shrubs cover a small part of the basin (0.38%, i.e., <1.4 km^2) only, erroneous mixing with e.g., grass is less of a problem, since grass and shrubs show similar LAIs here.

4.1.2.2. Glacier Albedo

We derived glacier albedo values from Landsat 8, "LS8," and Sentinel 2, "ST2," following the approach of Ren et al. (2021) (Text S4.3 in Supporting Information S1) and compared them to simulated mean glacier albedo values (excluding debris-covered areas) per 200 m elevation band (Figure 3b). Modeled glacier albedo reproduces the seasonal cycle at lowest elevation (4,800–5,000 m.a.s.l.), with alternating bare ice and snow-covered glacier

Figure 3. Comparison of observed and modeled variables at the distributed scale. (a) Monthly mean (±1 SD) leaf area index as modeled (black line) and measured (VIIRS) for all cells with grass (86.8 km^2; 3,650–5,780 m.a.s.l.), shrub (1.3 km^2; 3,760–4,790 m.a.s.l.), and larch (1.9 km^2; 3,700–4,420 m.a.s.l.). (b) Monthly mean glacier albedo (excluding debris-covered areas) as modeled (black line) and observed (Landsat 8, "LS8," in red; Sentinel 2, "ST2," in blue) for three specific elevation bands (±1 SD) at the approx. Equilibrium line altitude as well as below and above. (c) Monthly mean snow-covered fraction as modeled (black line) and observed (MODIS in blue; ±1 SD) for the entire upper Langtang Valley catchment. For the modeled snow-covered fraction, only cells with an average monthly snow depth ≥0.02 m were considered. (d) Comparison of modeled and observed (ECOSTRESS) surface temperatures averaged per land cover type (symbols) for different points in time. Colors indicate the elevation. Red shade indicates the target simulation period (hydrological year 2018/2019) used to calculate the model performance (R^2 and RMSE).

surfaces (RMSE of 0.17 for LS8 and 0.24 for ST2, respectively; Figure 3b). The modeled glacier albedo in the uppermost zones of the catchment (>6,000 m.a.s.l.) gives a slight bias compared to the LS8 observations and matches the ST2 data well especially during winter, which points to the discrepancy between the two remotely sensed products and associated uncertainties (Ren et al., 2021).

4.1.2.3. Snow-Covered Area

Monthly averages of simulated snow-covered fraction were compared to satellite-derived values (MODIS-Terra; Text S4.4 in Supporting Information S1) for the entire upper Langtang Valley (Figure 3c). We applied a snow depth threshold (monthly average per grid cell) of 0.02 m to calculate the modeled snow-covered fraction, as smaller snow amounts are likely not recognized in the remote sensing observations (Parajka & Blöschl, 2008). The model captured the timing of the winter/spring peaks in snow-covered area in 2019 but overestimated the total snow cover after the peak, leading to a snow cover fraction ∼20% too high in summer 2019 ($R^2 = 0.30$; RMSE = 0.21; Figure 3c).

4.1.2.4. Land Surface Temperature

Surface temperature, measured over diverse land surface types and over relatively large areas beyond single points, is an important variable to assess the validity of the modeled surface energy balance and especially the turbulent heat exchange between different surfaces and the atmosphere. For the time steps with available satellite-derived surface temperature (ECOSTRESS; Text S4.5 in Supporting Information S1) observations, we compared simulated surface temperatures averaged per land cover class over the entire study basin to the observed land surface temperature averaged over the same area (Figure 3d). The observed and modeled surface temperatures generally match ($R^2 = 0.77$; Figure 3d). A clear bias occurs for clean-ice glacier surfaces, for which the model estimates surface temperatures between −5°C and 0°C most of the time, whereas the remotely sensed temperatures show a much larger spread (between −20°C and 0°C). However, ECOSTRESS has been shown to have a sensor bias related to cold surfaces and very high elevations (Hulley et al., 2021; Weidberg et al., 2021) for which it is not calibrated and therefore is associated with relatively large uncertainties.

4.1.2.5. Discharge

We compared observed with modeled discharge at three stations (stream gauges Langtang Glacier at 4,419 m.a.s.l., Langshisha at 4,000 m.a.s.l., and Kyanjing at 3,850 m.a.s.l., indicated with IDs no. 15, 13, and 3, respectively, on the map; Figure 4). Discharge was measured with water level sensors (pressure transducers) and flow rating curves were established using rhodamine (Langtang) and salt dilution (Langshisha and Kyanjing) measurements at all three sites. Constrained by the duration of field campaigns (Langtang Glacier gauge) or sensor failures (other two sites), the discharge estimates only cover limited time windows during the model period. The most complete reference data set, below Langtang Glacier (Figure 4a), covers the period May–October 2019 and therefore includes both low flow (premonsoon) and high flow (monsoon) and shows the best match with the modeled discharge at this site. Here, *T&C* slightly underestimates streamflow compared to the observations (RMSE = 3.9 m^3 s^{-1}). The same is true for the Langshisha gauge site (Figure 4b; RMSE = 1.3 m^3 s^{-1}), where only parts of high-flow conditions in 2018, i.e., in the model spin-up period, are recorded. One possible reason for the underestimation here could be the retention of melt water in the debris-cover as well as supraglacial ponds on the two respective glaciers (E. S. Miles et al., 2017; Steiner, Kraaijenbrink, et al., 2021). Instead, the model overestimates the flow at the Kyanjing gauge site (Figure 4c; catchment outlet; RMSE = 9.9 m^3 s^{-1}) slightly in premonsoon 2019 (target model period). Note that the hydrological year 2017/2018 (white background in Figure 4c) belongs to the model spin-up period. The mismatch at the lowest stream gauge site can have various reasons: (a) overestimation of precipitation amounts during winter or spring (snow) and monsoon (rain); (b) overestimation of snow melt in the spring season; (c) underestimation of losses to groundwater (i.e., infiltration into fractured rock) or into geomorphic features (i.e., talus slopes or moraines) in the valley bottom of the watershed. Additionally, since measurements in this environment are extremely challenging (relatively unconstrained river beds due to unconsolidated material) and flow rating curves extrapolated to high-flow periods rely on observations during low-flow conditions, there are uncertainties in the gauged records, especially during the monsoon high-flow periods.

4.1.2.6. Glacier Surface Mass Balance

We generated elevationally resolved specific glacier mass balances derived by solving the continuity equation (indicated as "*Remote sensing inferred*" hereafter; E. Miles et al., 2021; Text S4.6 and Figures S8 and S9 in
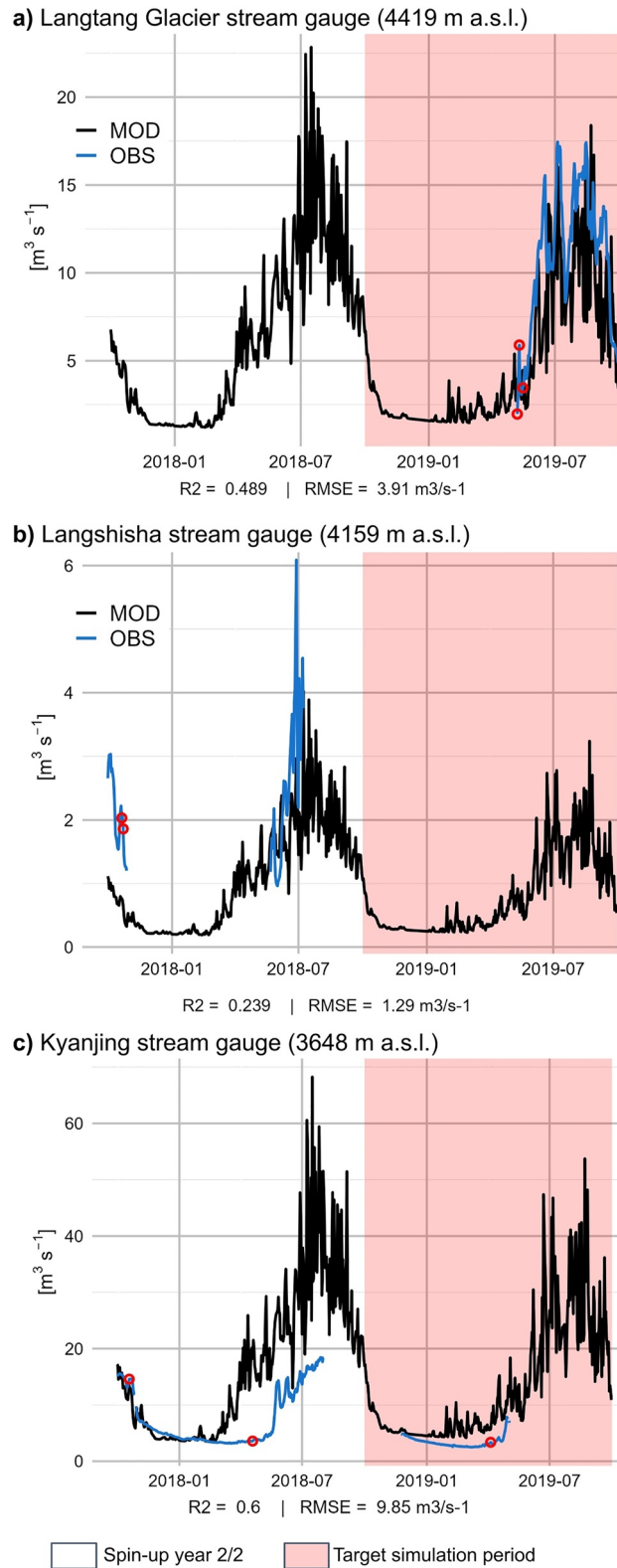
Figure 4. Observed and modeled mean daily discharge at Langtang Glacier (a), Langshisha (b), and Kyanjing (c) stream gauges, respectively. Red circles indicate days of rating curve measurements. Note that the first year (white background, hydrological year 2017/2018) belongs to the model spin-up period.
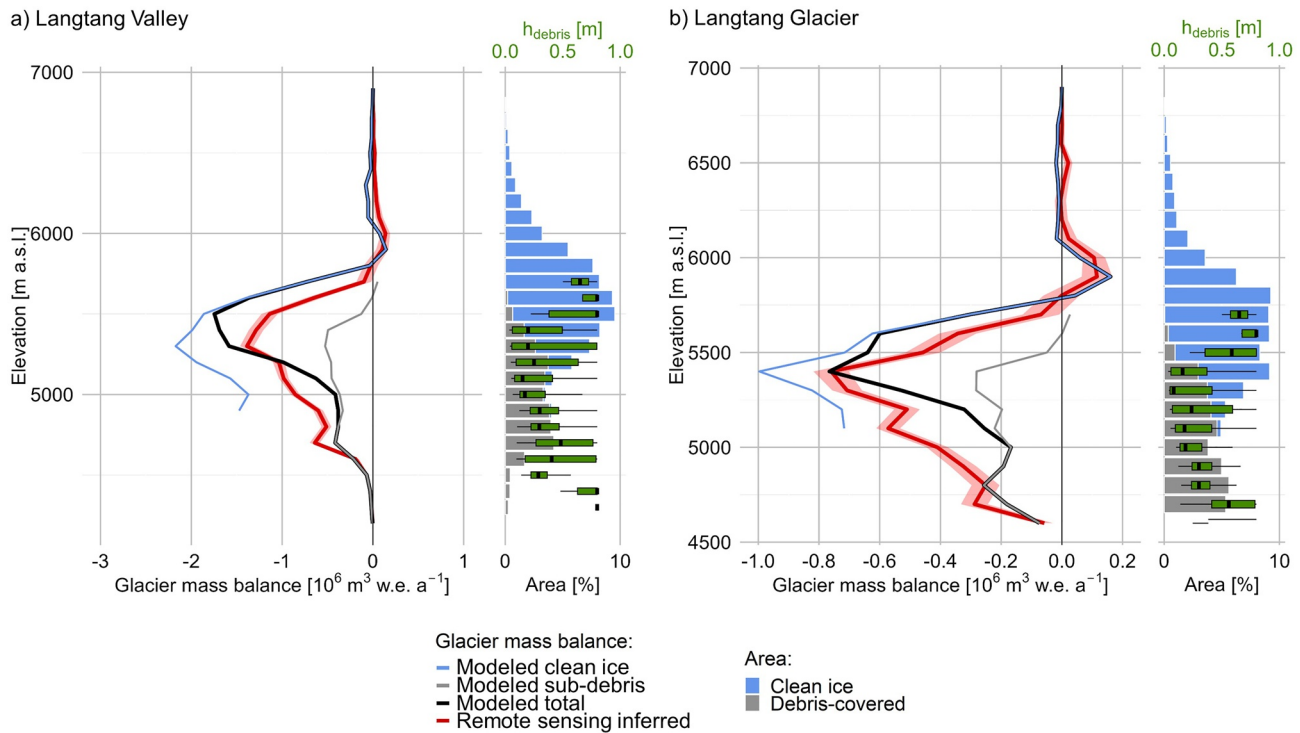
Figure 5. Elevation-resolved (averaged per 100 m elevation band) annual total glacier mass balance (line plots; average between postmonsoon 2017 and postmonsoon 2019), clean ice-covered and debris-covered area (bar plots) and debris thickness (boxplots) for the entire Langtang Valley watershed (a; see Figure S7 in Supporting Information S1 for spatial coverage) and individually for Langtang Glacier (b). The black line (*Modeled total*) and red line (*Remote sensing inferred*; shaded area: uncertainty range) indicate modeled and continuity equation-inferred specific glacier mass balances, respectively. The blue line (*Modeled clean ice*) and the gray line (*Modeled subdebris*) indicate average mass balances from clean ice and debris-covered areas, respectively.

Supporting Information S1). We compared the mean annual mass balance for the period 2017 until 2019 to the simulated monthly mass balance for the same period for all glaciers (Figure 5a; see Figure S7 in Supporting Information S1 for spatial coverage), as well as individually for Langtang Glacier (Figure 5b) which is the largest glacier in the catchment (46.5 km²; 43% of total glacier area). Results for the other main glaciers in the catchment are shown in Figures S16–S19 in Supporting Information S1.

The simulated and observed elevational profiles are generally consistent (Figure 5a): low mass loss toward the glacier terminus (<5,000 m.a.s.l.), where relatively thick debris-cover dominates and suppresses melt; and increasing mass loss at higher elevations, in the upper ablation zone (>5,000 m.a.s.l.), characterized by relatively thin debris-cover, marking the (actual, short-term) equilibrium line altitude of the glaciers in the catchment around 5,800 m.a.s.l. Both the catchment-scale and glacier-scale comparisons show a discrepancy between remote sensing inferred and modeled ablation patterns in the debris-covered ablation zone, where the model shows less annual ablation than is inferred from the satellite-derived estimates. Like the other main glaciers in the valley, Langtang Glacier has a heavily debris-covered tongue with supraglacial ice cliffs and ponds (Kneib, Miles, Buri, et al., 2021; Kneib, Miles, Jola, et al., 2021; E. S. Miles et al., 2017; Steiner et al., 2019) which locally enhance glacier melt (Buri et al., 2021; E. S. Miles et al., 2018) and lead to increased glacier thinning rates in areas of high density of these features (Ragettli, Bolch, et al., 2016). The mass loss effects of cliffs and ponds on the glacier surface are not included in the model and are also not represented in the debris thickness. The difference in modeled and estimated glacier mass balance in the upper parts of the debris-covered tongues is potentially a result of enhanced melt from supraglacial features, overestimated debris thickness or spatially variable physical debris properties.

4.2. Spatial Variability of Energy and Mass Fluxes

In this section, we show the distributed patterns of key atmospheric, cryospheric, and hydrological variables to explain the most important spatial characteristics of energy and water fluxes in the catchment.

4.2.1. Key Atmospheric Variables

Annual average net radiation (R_{net}; catchment average: 69 W m^{-2} h^{-1}; Figure 6a and Table S5 in Supporting Information S1) and sensible heat fluxes (H; catchment average: 31 W m^{-2} h^{-1}; Figure 6b and Table S5 in Supporting Information S1) are both largely influenced by the elevation (gradient in air temperature and incoming longwave radiation), the topography (exposure to incoming shortwave radiation), and the transient conditions at the surface (reflection of incoming shortwave radiation; emission of longwave radiation). Evaporation and sublimation (E; catchment total: 286 mm a^{-1}; Figure 6c and Table 1) are generally limited by the availability of energy and therefore their distribution is largely determined by the different surface conditions. Generally high E values are simulated for low elevations as a result of (wet) soils, but also for high altitudes with frequent snow cover, where sublimation takes place.

4.2.2. Key Cryospheric Variables

The strong elevation dependence of solid precipitation (P_{snow}; catchment total: 1,310 mm w.e. a^{-1}; Figure 6e and Table 1) shows that solid precipitation occurred in the entire valley during the model period, but that the highest altitudes received about 6.5 times more P_{snow} ($\sim$2,000 mm w.e. a^{-1}) than the lowest altitudes ($\sim$300 mm w.e. a^{-1}). The annual amounts of snowmelt (M_{snow}; catchment total: 834 mm a^{-1}; Figure 6f and Table 1) increase with elevation and increased snow accumulation until the point at high altitude where it is decreasing again due to a lack of energy for melt. Highest annual ice melt (M_{ice}; catchment total: 180 mm w.e. a^{-1}; Figure 6g and Table 1) totals are apparent at the debris-covered tongues (low elevation) and at the transition from debris to clean ice (below the snowline altitude). The spatial pattern of evaporation and sublimation from snow and ice ($E_{snow/ice}$; catchment total: 165 mm w.e. a^{-1}; Figure 6h and Table 1) is elevation dependent due to dry and cold (nonmelting) conditions in combination with the availability of snow and ice surfaces being more likely at high elevations.

4.2.3. Key Hydrological Variables

While the absolute amount of water stored in the soil ($V_{soil\ water}$; catchment total: 96 mm w.e.; Figure 6i and Table 1) is controlled by the soil characteristics, and P and E rates, the transient spatial distribution is generally related to the lateral subsurface water flux (Q_{lat}; Figure 6k). Both $V_{soil\ water}$ and Q_{lat} show no elevation-dependency within the soil-dominated and vegetation-dominated lower regions of the catchment, but mirror the influence of assumed local topography on the routing of subsurface water pathways.

Strongly tied to the phenology and activity of the vegetated land cover, transpiration (Tr; catchment total: 26 mm w.e. a^{-1}; Figure 6j and Table 1) shows a clear elevational pattern within the lower half of the catchment (<5,000 m.a.s.l.), with decreasing transpiration rates with elevation.

Highest rates of evaporation and sublimation from interception on vegetation ($E_{intercept.}$; catchment total: 6 mm w.e. a^{-1}; Figure 6l and Table 1) are simulated for the larch sites (because of higher LAI) where higher volumes of leaf intercepted water are available for longer periods to eventually evaporate, compared to the grass and shrub areas.

4.3. Sub-Seasonal Mass Fluxes

We analyzed the modeled mass fluxes during the 2019 hydrological year and extracted monthly averages (in mm w.e. mo^{-1}) per 100 m elevation band (Figure 7). For a given month, we summed a specific variable (e.g., M_{snow}) over all cells per elevation band, and divided that sum by the number of cells in that elevation band (i.e., total M_{snow} per altitudinal band, divided by area, resulting in an "effective" or "specific" melt rate). Average mass fluxes per elevation band derived in this way show the importance of a particular water balance component in relation to other components at a specific elevation. We first present the bulk mass fluxes for the major hydrological balance components (precipitation, snow and ice melt, total ET; Figures 7a–7d) and then examine the individual ET components (Figures 7e–7h). The latter, in combination, all result in the direct loss of water from the catchment without contributing to runoff.

4.3.1. Precipitation (P)

The main share of P in the modeled period fell during the monsoon season (July and August 2019; Figure 7a) as liquid precipitation generally below 5,000 m.a.s.l. (Figures S20 and S23a in Supporting Information S1). February 2019 ranked directly after August and July in terms of total P (Figure 7a and Table 1), while in the
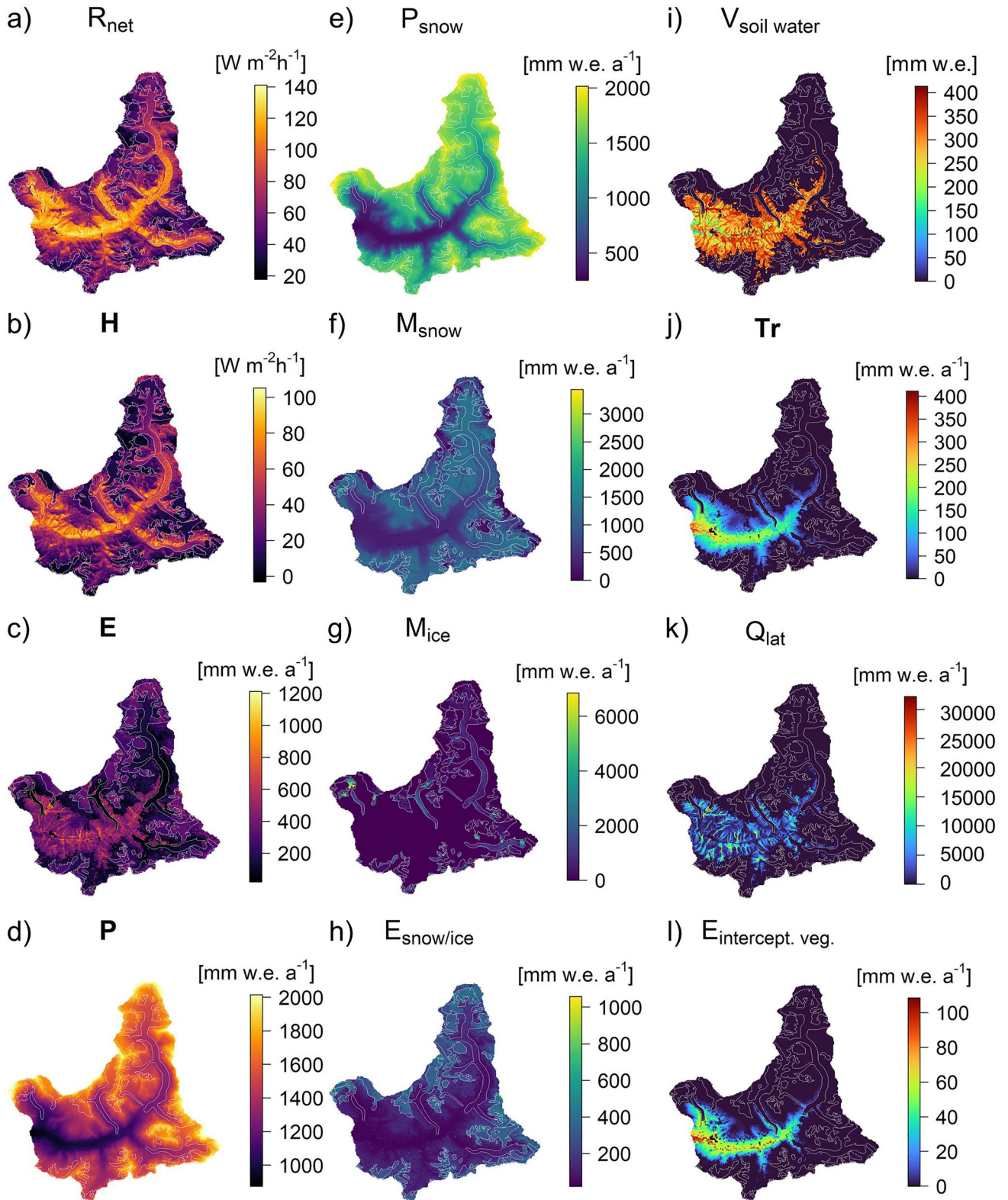
Figure 6.

Table 1
Annual and Monthly Total Values of the Water Balance Components Calculated for the Upper Langtang Catchment for the 2019 Hydrological Year

	Annual	Oct	Nov	Dec	Jan	Feb	Mar	Apr	May	Jun	Jul	Aug	Sep
Variables	[mm w.e. a^{-1}]					[mm w.e. mo^{-1}]							
Precipitation	**1467.4**	**0.5**	**3.1**	**0.3**	**71.9**	**218.8**	**49.3**	**109.8**	**70.2**	**162.8**	**250.7**	**313.7**	**216.4**
Snow	1309.8	0.5	3.0	0.3	71.9	218.8	49.3	109.2	68.5	140.6	200.8	257.3	189.6
Rain	157.6	0.0	0.1	0.0	0.0	0.0	0.0	0.5	1.7	22.2	49.8	56.4	26.8
Snow melt	**834.4**	**3.1**	**2.4**	**0.3**	**13.3**	**33.3**	**43.0**	**59.2**	**82.4**	**137.3**	**156.7**	**181.5**	**121.9**
Ice melt	**180.1**	**37.7**	**9.1**	**0.9**	**6.7**	**0.6**	**3.1**	**8.8**	**18.3**	**30.2**	**26.7**	**22.3**	**15.5**
Bare-ice	120.1	30.6	7.3	0.7	6.7	0.6	3.0	6.3	10.5	17.1	15.1	12.9	9.3
Sub-debris	59.9	7.1	1.8	0.2	0.0	0.0	0.2	2.5	7.8	13.1	11.6	9.4	6.2
Evapotranspiration	**285.8**	**18.5**	**11.2**	**8.8**	**12.9**	**17.9**	**33.6**	**40.2**	**44.3**	**32.5**	**22.7**	**24.8**	**18.5**
Transpiration	26.0	1.9	0.3	0.0	0.0	0.0	0.0	0.8	2.9	4.9	5.0	6.1	4.2
Soil	63.5	6.1	1.9	0.4	0.1	0.6	3.9	9.1	12.2	11.0	7.4	6.6	4.2
Interception	6.3	0.0	0.0	0.0	0.0	0.0	0.0	0.0	0.0	0.3	1.9	2.1	1.9
Standing water	26.0	0.8	0.2	0.0	0.1	0.6	3.0	4.0	4.8	3.7	3.1	3.9	1.8
Ice	24.6	6.0	6.2	6.1	3.6	0.1	0.4	0.5	0.8	0.5	0.1	0.1	0.1
Snow	139.3	3.7	2.6	2.1	9.1	16.6	26.2	25.8	23.6	12.0	5.2	6.0	6.3
Runoff	**1210.3**	**73.1**	**40.8**	**36.7**	**37.4**	**40.2**	**48.6**	**64.9**	**88.1**	**164.3**	**212.1**	**246.0**	**158.1**
	[mm a^{-1}]					[mm mo^{-1}]							
Soil water storage	**95.6**	**82.7**	**78.2**	**77.2**	**78.2**	**90.5**	**100.8**	**106.1**	**103.5**	**103.4**	**107.9**	**110.2**	**109.1**
Liquid	64.8	78.7	55.4	32.4	10.5	15.9	27.7	54.9	78.5	97.6	107.2	110.1	109.1
Frozen	30.8	4.0	22.8	44.8	67.7	74.6	73.1	51.2	25.0	5.8	0.7	0.1	0.0

Note. The greatest magnitude individual water balance, *ET*, and soil water storage components for each month are highlighted in blue, green, and yellow, respectively.

40 years average (based on *ERA5-Land* data) February ranked as the seventh highest *P* month (Figure S21c in Supporting Information S1). Monthly *P* totals in July and August 2019 ranged from 169 to 211 mm w.e. mo^{-1} at 4,000 m.a.s.l. to 340–425 mm w.e. mo^{-1} at 6,600 m.a.s.l., respectively.

4.3.2. Snowmelt (M_{snow})

Winter M_{snow} is most pronounced at the lowest elevations of the study area and progresses toward higher altitudes with the onset of the melting season in the premonsoon season (Figure 7b). The highest M_{snow} rates for the main months during the melting season (May to September) range from 173 mm w.e. mo^{-1} in May to 276 mm w.e. mo^{-1} in August and are all found in a relatively narrow elevational range between 5,100 and 5,400 m.a.s.l. Average annual M_{snow} totals peak in that elevational zone regardless of terrain aspect, but are higher for the south facing slopes (ESE-WSW) than north-oriented surfaces (Figure S22 in Supporting Information S1) as observed also in a previous observational study (Girona-Mata et al., 2019).

4.3.3. Ice Melt (M_{ice})

At the onset of the melt season, the highest M_{ice} rates are found at 4,700 m.a.s.l. in May 2019 (43 mm; Figure 7c), whereas M_{ice} rates consistently peak at an elevation of 5,300 m.a.s.l. between June and September 2019, ranging between 37 (September) and 63 mm w.e. mo^{-1} (July) for that particular elevational band. The highest M_{ice} rates overall, though, are simulated for October 2018 with an average of 99 mm w.e. mo^{-1} at the 5,500 m.a.s.l. elevation band.

Figure 6. Selected distributed model outputs shown as annual averages (radiative fluxes) or totals (mass fluxes) for the 2019 hydrological year (1 October 2018–30 September 2019) in the upper Langtang Valley. (a–d) Key land-surface variables regarding atmospheric and surface conditions: net radiation (R_{net} [W m^{-2}]), sensible heat (H [W m^{-2}]), latent heat (E [mm w.e. a^{-1}]), precipitation (P [mm w.e. a^{-1}]); (e–h) key cryospheric variables (all in mm w.e. a^{-1}): snowfall (P_{snow}), snow melt (M_{snow}), ice melt (M_{ice}), evaporation and sublimation from snow and ice ($E_{snow/ice}$); (i–l) key variables concerning hydrology (all in mm w.e. or mm w.e. a^{-1}): water stored in the soil ($V_{soil\ water}$), transpiration (Tr), incoming lateral subsurface water flux (Q_{lat}), evaporation and sublimation from intercepted water and snow from vegetation ($E_{intercept}$).
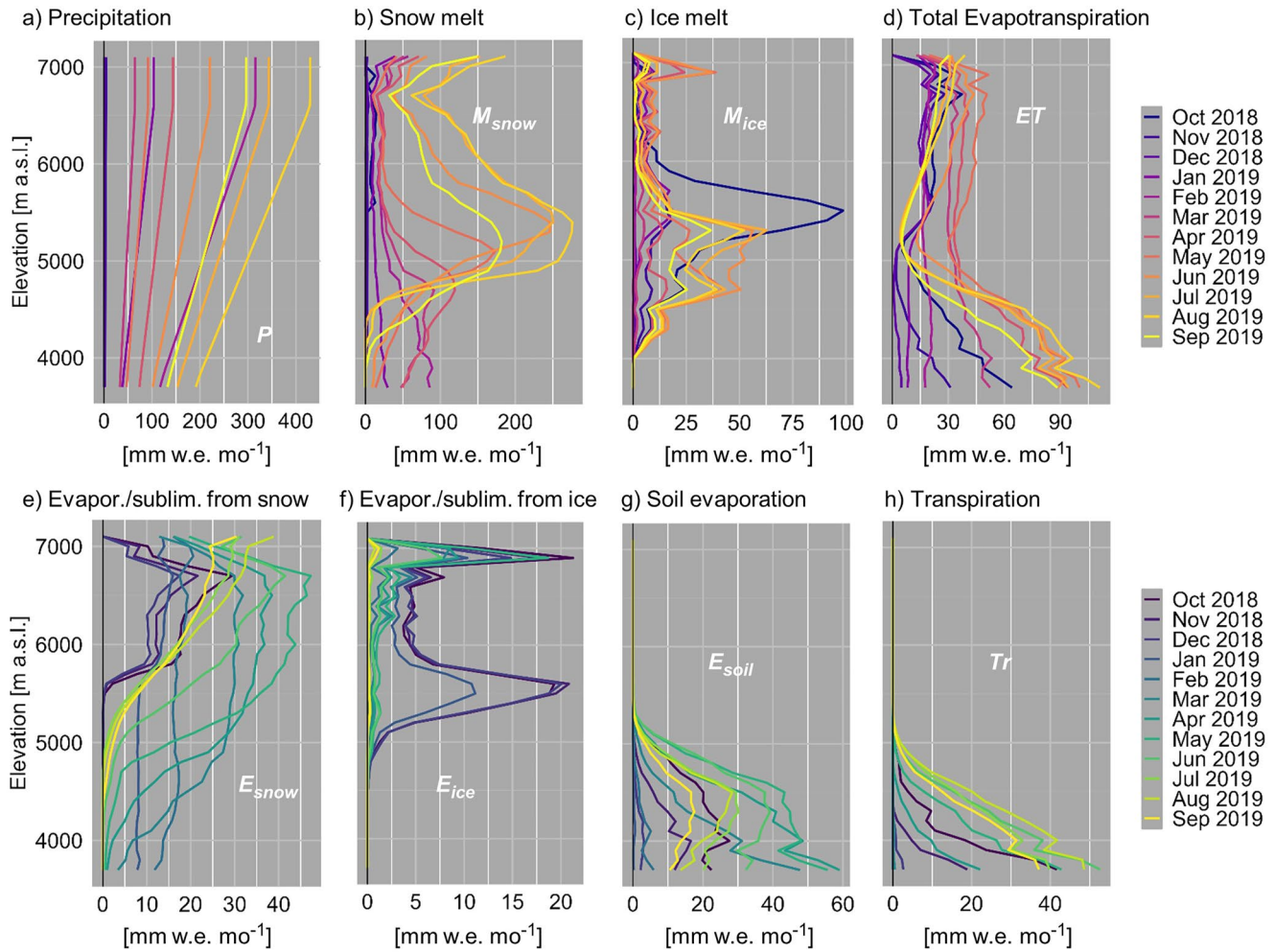
Figure 7. Elevational distribution of monthly average mass fluxes (averaged over all cells in an elevation band) as modeled for the 2019 hydrological year for the upper Langtang Valley catchment. The top panel (a–e) shows the main mass flux components relevant for the catchment water balance, the bottom panel (e–h) consists of the various *ET* components. Positive values in subplots d–h indicate net vapor mass fluxes from the surface to the atmosphere (evaporation, sublimation, or transpiration).

4.3.4. Evapotranspirative Fluxes (*ET*)

The majority of the months of the hydrological year 2018/2019 show distinct peak *ET* rates at the highest and lowest elevation bands (Figure 7d). Looking at the modeled individual *ET* fluxes (Figures 7e–7h show the most important ones for the water balance), the high magnitudes toward the uppermost and the lowermost altitudes of the study catchment are a consequence of the complementary behavior of evaporation and sublimation from snow and ice (E_{snow} and E_{ice}; high elevation) and the other three main *ET* components, i.e., evaporation from ground (E_{soil}), evaporation from standing water (E_{pond}), and transpiration (*Tr*; all at low elevation).

E_{snow} is the main contributor to the total *ET* water loss to the atmosphere at elevations above 5,500 m.a.s.l. (Figure 7e; 86%), whereas evaporation and sublimation from ice (E_{ice}) are only minor contributors above 5,500 m.a.s.l. in the study catchment (Figure 7f; 14%). E_{soil} is the primary *ET* mass flux at low elevations (<5,000 m.a.s.l.; 43%) in the catchment (Figure 7g), followed by *Tr* (19%) in that particular elevation range. The vegetation in the study catchment transpires at the highest rates (∼50 mm w.e. mo^{-1}; Figure 7h) between June and August, marking the onset and peak of the monsoonal season, respectively.

4.4. Annual Mass Balance Partition

The average partition along the elevation gradient (Figures 8a and 8d) emphasizes the importance of an individual component compared to the others at a given elevation and allows to compare the magnitude of a given flux per
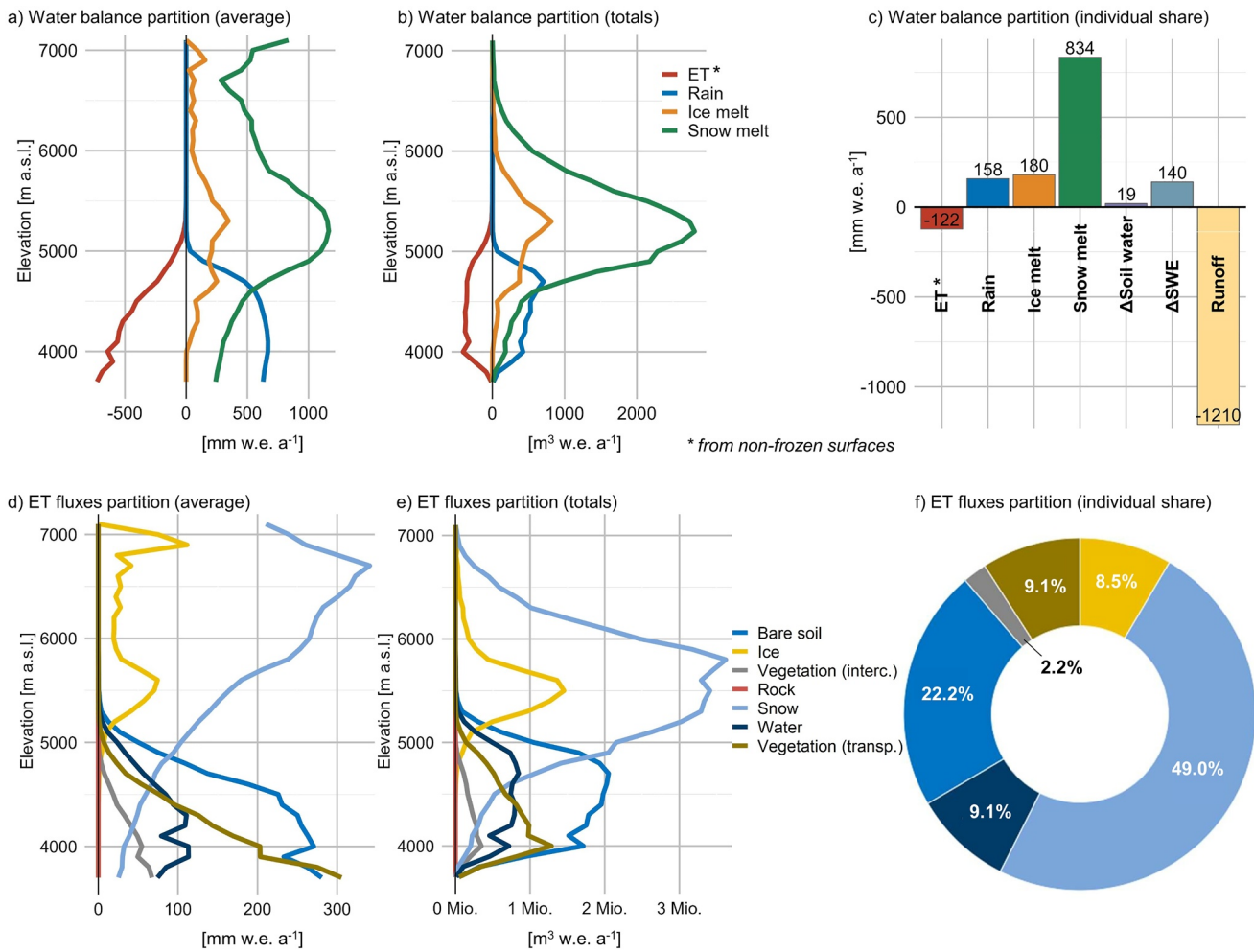
Figure 8. Partition of (liquid) water balance (a–c; here vapor fluxes directed from the surface to the atmosphere are shown as negative values; note that *ET* is excluding snow and ice surfaces here) and *ET* mass fluxes from all surfaces (d–f) as averages (averaged over all cells in an elevation band), area-weighted totals and catchment-wide totals, respectively, per elevation band for the 2019 hydrological year. (a) Elevation-resolved average water balance partition; (b) elevation-resolved, area-weighted water balance partition; (c) catchment-wide water balance partition; Δ*Soil water* and Δ*SWE* are the storage changes for water in the soil and in the snow pack, respectively. (d) Elevation-resolved average *ET* partition; (e) elevation-resolved, area-weighted *ET* partition; (f) catchment-wide *ET* partition.

unit area at different elevations, while the (area-weighted) totals reveal the absolute relevance of each component for the total catchment water balance at a given elevation (Figures 8b and 8e) or at the catchment scale (Figures 8c and 8f).

Noticeable differences in the general elevational distribution between the individual water balance components appear when examining their annual averages (Figure 8a). Here, we are looking at the (liquid) water balance from a runoff perspective, i.e., based on whether a component is contributing to runoff (rain, ice melt, snow melt) or removing it (runoff, *ET* from nonfrozen surfaces). In terms of inputs to the water balance, liquid precipitation clearly dominates the lowermost altitudinal zone (<4,600 m.a.s.l.) of the catchment, almost exclusively due to rain events during the monsoon season (Figure S20 in Supporting Information S1). Above 4,500 m.a.s.l., annual M_{snow} exceeds the amount of rain (P_{liq}), and at about 4,800 m.a.s.l., above which the occurrence of P_{liq} is very rare, the water generated from M_{ice} is more important for the water balance than rain. On the negative side of the water balance, the relative importance of the *ET* mass fluxes exceeds the input from P_{liq} in the lowermost elevations <3,900 m.a.s.l.

M_{snow} shows a bimodal altitudinal distribution with a large amplitude (ranging from 200 to 1,200 mm w.e. a^{-1}), peaking between 5,000 and 5,500 m.a.s.l. and to a lesser extent above 7,000 m.a.s.l. Similarly, the average M_{ice} rates are bimodally distributed with elevation and peak in the same altitudinal zone, but showing a considerably

smaller magnitude (ranging from 0 to 350 mm w.e. a^{-1}). In contrast, ET rates (excluding snow and ice surfaces here) show a minimum around 5,200 m.a.s.l., but increase toward the lower end of the catchment (Figure 8a).

Given the characteristic unimodal catchment hypsometry (Figure 1c) of the upper Langtang Valley with a distinct peak between 5,000 and 5,500 m.a.s.l., it is evident that this elevation range amplifies the overall importance of individual average water balance fluxes (Figure 8a) in an absolute manner (Figure 8b) at the catchment scale (Figure 8c). Consequently the two most important mass fluxes on average between 5,000 and 5,500 m.a.s.l. (Figure 8a), M_{snow} and M_{ice} are also contributing most to the catchment water balance across all elevation bands (Figure 8b) and show the largest share in the total catchment water balance (63% and 14% of all the positive water balance components, respectively; Figure 8c). The contribution of P_{liq} to the water balance (12%) is only slightly less than that of M_{ice}, but concentrated to a relatively narrow altitudinal zone of <1,500 m (3,650–5,100 m.a.s.l.) compared to the M_{ice} occurring over >3,000 m of altitude.

The absolute total amount of ET (including snow and ice surfaces) at the catchment scale (286 mm w.e. a^{-1}; Table 1) is 59% higher than the total M_{ice} (180 mm w.e. a^{-1}), which emphasizes the fact that it is not enough to focus on ice melt alone in assessing how much water is available to supply downstream regions. The bulk part of the water returned to the atmosphere through ET mass fluxes originates from the zone between 5,000 and 6,000 m.a.s.l., predominantly from snow and ice surfaces (Figure 8e). In the upper half of the catchment (>5,300 m.a.s.l.), where glacierized and rocky land cover with frequent snow cover dominate, $E_{snow/ice}$ make up the entire annual ET, with average E_{snow} and E_{ice} rates peaking at 6,700 and at 6,900 m.a.s.l., respectively (Figure 8d). Going toward lower elevations, where soils and vegetation are the dominant land covers and snow cover is less frequent, it is only below 5,000 m.a.s.l. that ET mass fluxes from nonfrozen surfaces become the dominant component: E_{soil} exceeds the annual total of E_{snow} below 4,800 m.a.s.l. (Figures 8d and 8e), followed by evaporation from ponded water in convergent portions of the landscape (E_{pond}; 4,600 m.a.s.l.), Tr (4,500 m.a.s.l.), and $E_{intercept.}$ (4,100 m.a.s.l.). In the lowest reaches of the catchment (<4,000 m.a.s.l.), which marks the upper limit of more dense vegetation in the Langtang Valley, vegetation becomes the dominant source of ET (both in relative and absolute terms; Figures 8d and 8e). At the catchment scale, the individual shares of the ET components (Figure 8f and Table 1) are dominated by E_{snow} (49%) and E_{soil} (22%), whereas Tr, E_{pond}, and E_{ice} show considerably smaller but similar contributions (about 9% each). $E_{intercept.}$ on vegetation contributes 2% to the annual ET.

4.5. Depletion and Regeneration of the Cryospheric Water Budget

When looking at the cryospheric variables P_{snow}, M_{snow}, $E_{snow/ice}$ as well as M_{ice} we can derive the spatiotemporal pattern of depletion and regeneration of the catchment cryospheric water budget (Figures 9a and 9b). The balance heatmap (Figure 9a) reveals a distinct replenishment of the cryospheric system in February (>5,500 m.a.s.l.) and during monsoon (>6,000 m.a.s.l.) through P_{snow} (Figure 9c) in the upper zone of the basin. Concurrently, M_{snow} (Figure 9e), M_{ice} (Figure 9d), as well as $E_{snow/ice}$ (Figure 9f) are responsible for the balance depletion in premonsoon (entire vertical extent) and monsoon (<6,000 m.a.s.l.). However, these three negative balance components act in very distinctive spatiotemporal zones. While the contribution of M_{snow} to the cryospheric budget depletion happens especially in the lower (February to April) and central altitudinal zone (May–September) of the catchment, $E_{snow/ice}$ acts in a complementary way, with high magnitudes during postmonsoon in the upper half of the catchment, and gradually increasing from low to high elevations from March to September. Although the magnitudes of M_{snow} are generally very high and crucial for the overall balance, especially in the lower half of the study basin, at high elevations it is mainly $E_{snow/ice}$ that causes a distinct change in accumulated snow (March to May) between winter and monsoon originating from P_{snow}. With the onset of the melt season and the decreasing snow cover in the lower reaches of the catchment, large elevational gradients of E_{snow} rates occur from April to June, indicating a suppression by monsoon later in the ablation season.

5. Discussion

5.1. Importance of Evapotranspiration for the Water Balance

Our simulations reveal that the equivalent of >1.5 times the total amount of ice melt production is lost directly to the atmosphere through evapotranspirative fluxes (during the 2019 hydrological year; Table 1), and does not contribute to catchment runoff and downstream water availability. We found that it is primarily sublimation from snow at high elevations and ET from soil and vegetation at low elevations (Figure 8d) that determine the relative
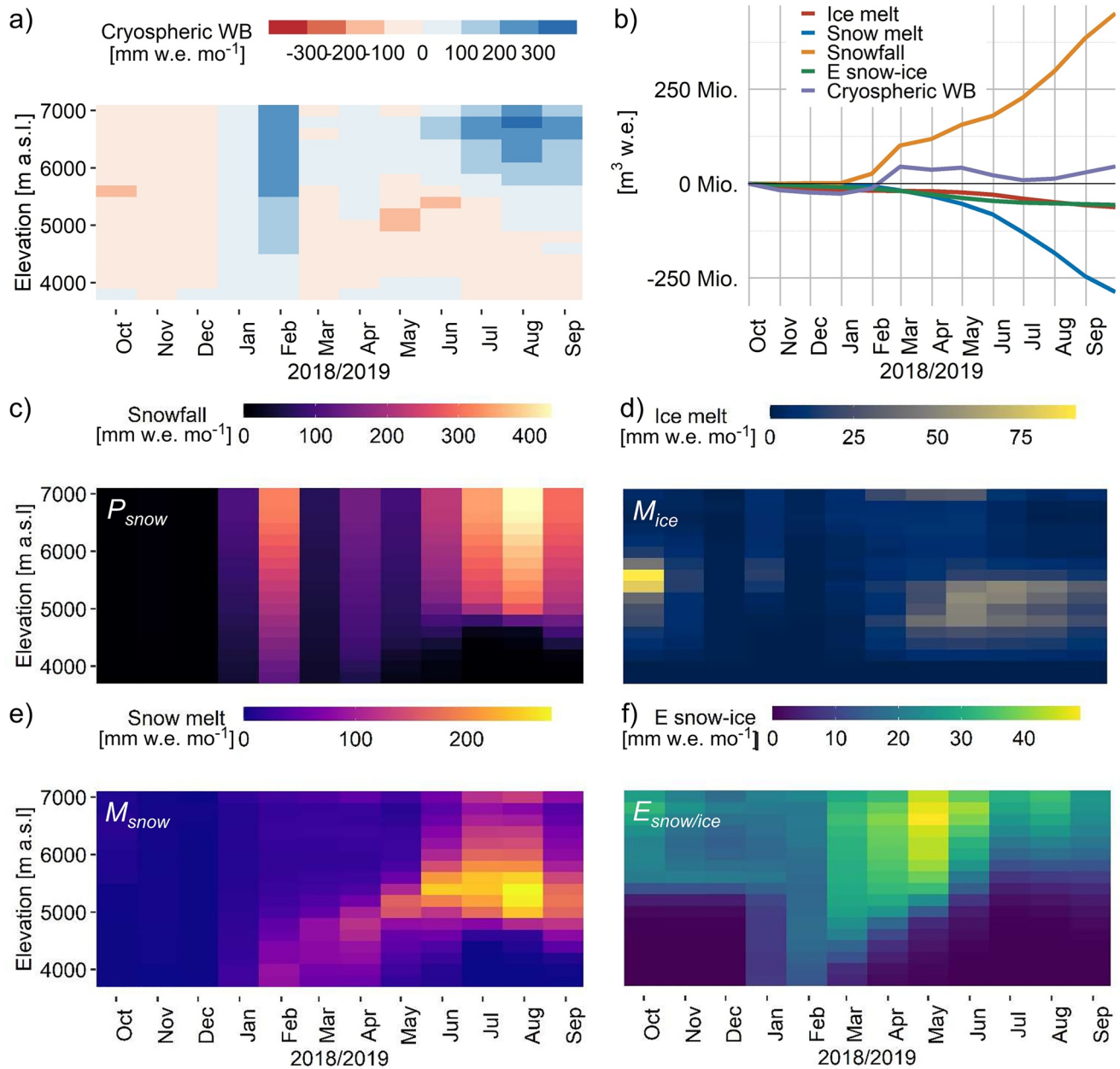
Figure 9. Spatio-(elevation bands) temporal (monthly averages) heatmap of the cryospheric water balance (WB = snowfall − snow melt − ice melt − snow/ice evaporation) for the hydrological year 2018/2019 (a; mm w.e. mo⁻¹), time series of cumulative water balance and individual components for the same period (b; m^3 w.e.), and individual spatiotemporal heatmaps for snowfall (c), ice melt (d), snow melt (e), and snow and ice sublimation (f), respectively (all in mm w.e. mo⁻¹).

importance of latent heat fluxes for the total water balance in the Langtang Valley. To our knowledge our study is the first one in HMA that provides catchment-scale estimates of diverse vapor fluxes, enabling us to establish their relative importance for the water balance of a Himalayan catchment. We estimated snow sublimation to account for the equivalent of 11% of snowfall, 17% of snowmelt, and 77% of ice melt, respectively, at the annual and catchment scale (Table 1).

Point observations from the Langtang (Stigter et al., 2018; 5,350 m.a.s.l.) and the Chhota Shigri catchments (Mandal et al., 2022; 4,863 m.a.s.l.; Western Himalayas) showed that snow sublimation can account for between 16% and 42% of the total winter snowfall at those given locations. At the scale of the entire Indus basin, Gascoin (2021) estimated snow sublimation from remote sensing products to account for 11% of the annual snowmelt. Here, we fill this clear scale gap between point and very large scale HMA estimates. Our

simulations reinforce the findings of previous studies (e.g., Gascoin, 2021; Mandal et al., 2022; Pradhananga & Pomeroy, 2022; Sherpa et al., 2023; Stigter et al., 2018) that understanding the processes of evaporation and sublimation from frozen surfaces is crucial in glacierized, high-elevation catchments, as snow and ice melt alone do not provide the entire picture of the cryosphere-related water fluxes (Figure 9).

Whereas evaporation and sublimation from snow overall dominates and makes up almost half (49%; Figure 8f) of the total *ET* flux at the catchment scale in 2019, transpiration and interception from vegetation accounts for >11% of total *ET*, as only one quarter of the basin area is vegetated (mostly grassland) and the most productive vegetation types (larch and shrub) cover <1% of the catchment area. As the vegetation below the study basin boundary at 3,600 m.a.s.l. further densifies with prevalent forests (Beug & Miehe, 1999) and as temperature rises with decreasing elevation, it is expected that the relative importance of transpiration will increase downvalley.

Flux tower measurements at high elevations are very rare and estimates of *ET* fluxes are thus difficult to validate directly. *ET* modeled with *T&C* has been validated with flux tower measurements at alpine sites in the European Alps in Switzerland (Davos, 1,639 m.a.s.l.) and Italy (Lavarone, 1,139 m.a.s.l.; Monte Bondone, 1,550 m.a.s.l.; Renon 1,730 m.a.s.l.; Torgnon, 2,160 m.a.s.l.), as well as two sites in the interior western USA (Reynolds Creek, Idaho, ~2,100 m.a.s.l.) over different vegetation types with satisfying results (Botter et al., 2021; Fatichi et al., 2012a; Mastrotheodoros et al., 2020). For instance, Reba et al. (2012) reported 42 and 17 mm a^{-1} (period 2004–2006) of snow sublimation at the two sites in the Reynolds Creek watershed, that were previously modeled by *T&C* (54 and 8 mm a^{-1}, period 1983–2008; Fatichi et al., 2012a). Here, we simulated October to November sublimation rates of 0.96 and 1.45 mm d^{-1} for the years 2017 and 2018, respectively, at the AWS Yala Glacier site (5,350 m.a.s.l.) which is in agreement with flux tower measurements during postmonsoon at the same location ranging between 1 and 1.5 mm d^{-1} (15 October–17 November 2016; Stigter et al., 2018). Direct *ET* measurements from flux towers and lysimeters at similar elevations on the Tibetan Plateau (ca. 750 km north, between 3,500 and 5,000 m.a.s.l.) find rates between 1 and 3 mm d^{-1}, during the summer months (Chang et al., 2017; Wang et al., 2020). For the 7,000-m elevation band in the Langtang catchment, we simulated October to November sublimation rates of 0.8 and 1.0 mm d^{-1} for the years 2017 and 2018, respectively, which is similar to the results of Sherpa et al. (2023) who estimated 1.1 mm d^{-1} on average for the period October–November in 2019 and 2020 based on station data from Everest's South Col at 7,945 m.a.s.l. Overall, despite recognized uncertainties, multiple sources of evidence suggest that simulated evaporation and sublimation fluxes are realistic.

Several satellite products provide *ET* estimates of high spatial resolution over HMA (e.g., Chen et al., 2014; Fisher et al., 2020; Jung et al., 2019; Martens et al., 2017; Mu et al., 2011; Yuan et al., 2021; Zhang et al., 2019). However, satellite-borne calculations or estimates of *ET* based on thermal imagery usually do not distinguish between land surfaces with snow and ice cover (sublimation) and those without, and hence fail to capture the spatial patterns of *ET* in mountainous regions, despite a relatively high spatial resolution (e.g., *MOD16* or *PML-V2*; 500 m spatial resolution; He et al., 2022). In addition, spatiotemporally continuous time series of *ET* are almost impossible in some regions, as clouds frequently inhibit thermal sensing of the Earth's surface from space, e.g., in HMA (Zhao et al., 2005). We compared *T&C*-simulated monthly catchment averages of total *ET* for the hydrological year 2018/2019 to the *ET* derived from reanalysis (ERA5-Land; ~9-km spatial resolution; Muñoz-Sabater, 2019) and satellite data (GLEAM v3.7b; ~25-km spatial resolution; Martens et al., 2017) and found agreement of the *T&C* estimates (spatially averaged over 35,000 cells) with those of ERA5-Land (4 cells), but disagreement with GLEAM v3.7b (1 cell) both in terms of seasonality and annual sums (Figure S25 in Supporting Information S1). The comparison shows that our mechanistically derived estimates of *ET* are in the right order of magnitude at the catchment scale. However, despite the agreement with the reanalysis estimate we believe that the spatial resolution of reanalysis and satellite products (providing spatiotemporally continuous *ET* products) or nonmechanistic models cannot quantify the latent heat fluxes that originate from a variety of spatiotemporally variable land surfaces in complex mountain terrain (e.g., Rouholahnejad Freund & Kirchner, 2017). Most importantly, reanalysis could never be used for simulating future scenarios.

5.2. Influence of Catchment Hypsometry on the Water Balance

The total amounts of snow melt, ice melt, and *ET* in the central altitudinal zone (5,000–5,500 m.a.s.l.) are the determinants of the annual catchment water balance (Figures 8b and 8c). The hypsometry of the catchment (Figure 1b) determines the relevance of this midsection for the hydrological budget, as the high relative share of (planimetric) surface area in that zone (hypsometric peak area) means that this zone can accumulate high

amounts of precipitation. In addition, environmental (temperature) and topographical (slope) conditions in this central zone of the catchment allow for the presence of glacier ice and a transient snow cover, which can melt or be vaporized.

A basin with different geomorphologic properties can be expected to produce a considerably different water partitioning (e.g., Vivoni et al., 2008). For example, a catchment with large area in a lower altitudinal zone (e.g., ∼4,500 m.a.s.l.) would be characterized by a smaller snow-covered area and a higher share of soils and vegetation at the cost of glacier ice and rock surface, and thus a lower overall importance of snowmelt and a higher impact of rain (primarily temperature dependent) and transpiration (primarily land cover dependent) could be expected. The distribution of glaciers in the catchment is also crucial for its water balance. Notably, the presence of supraglacial debris has a strong effect on the elevational distribution of ice melt, as it shifts the peak melt rates toward higher elevations and allows the survival of glacier ice below the termini of clean-ice glaciers, due to its enhanced insulation (e.g., Rowan et al., 2015). The catchment hypsometry is also crucial to modulate the effect of a warming climate on catchment water balance and fluxes partition: a future rise in temperature, accompanied by higher snow lines and reduced snow-covered areas will shift the peak rates of snowmelt and vapor fluxes from snow toward higher elevations and therefore above the hypsometric peak area of the catchment, decreasing the importance of these mass fluxes for the catchment water balance. Larger sections of the catchment will experience rain, and the subdebris and clean-ice glacier melt will likely accelerate. With retreating and disappearing glaciers tongues, evaporation from bare soil and potentially vegetation will increase. However, it remains unclear if total *ET* would increase or decrease in such a scenario and by how much. Land surface modeling studies in catchments with distinct hypsometry and glacier distribution and into the future thus seem important to unravel the complexity of fluxes partition in high-elevation catchments and provide a full picture on the water cycle of HMA.

5.3. Representativeness of the Results

This study focuses on the 2019 hydrological year. To test how representative the water balance partition is, we place the 2019 catchment climatology into the context of its long-term climatology using ERA5-Land reanalysis data (Muñoz-Sabater et al., 2021). In 2019, higher than normal winter snowfalls occurred in the central Nepalese Himalayas, mostly determined by an extreme snowfall event in February 2019 (second highest ranked February total precipitation for the period 1980–2020; Figure S21c in Supporting Information S1). Little precipitation was recorded beforehand in the postmonsoon season (total precipitation of 3.8 mm w.e. for the period October–December 2018; Table 1), marking a dry start for the 2019 hydrological year. In addition, 2019 was a rather cold year (ranked seventh coldest mean annual air temperature from 1980 to 2020; Figure S21 in Supporting Information S1). Overall, 2019 was a year with high winter precipitation amounts and relatively cold average air temperatures, leading to overall lower ice melt volumes.

Due to the higher-than-average snowfall amount in February 2019, ice melt rates were suppressed in the glacier ablation zone in premonsoon 2019. More average winter snow conditions would likely decrease snowmelt totals and raise the annual ice melt amount. Warmer air temperatures would decrease snowfall and increase ice melt rates. Reduced snowfall generally lowers *ET* totals (due to less sublimation from snow), too, but the effect is less pronounced as a reduced availability of snow (in terms of area and depth) leads to decreased vapor fluxes from snow, but increases the potential for vapor fluxes from ice in glacierized zones and generally evapotranspirative mass fluxes from soil and vegetation further downvalley.

A number of hydrological modeling studies exist for other years in the upper Langtang Valley (e.g., Braun et al., 1993; Fukushima, 1991; Konz et al., 2007; Ragettli et al., 2015). We obtain differences in the amounts of snowfall, snowmelt, and runoff for different years (Table S6 in Supporting Information S1). The ratio of ice melt to snowmelt was simulated to be 0.22 in 2019 but 0.65 in 2013 (Table S6 in Supporting Information S1). These differences may be explained by the exceptional snowfall events in winter and monsoon 2019, which provided a considerably higher amount of snow to potentially melt and also contributed to higher runoff compared to the 2013 estimates.

An extended simulation period (>decade) would account for the interannual variability in meteorological forcing and allow to understand a more average hydrological behavior of the study catchment (e.g., Günther et al., 2019), but is currently hindered by the meteorological forcing and computational costs of our modeling approach (see section below).

5.4. Reflections on the Modeling Approach and Future Challenges

We apply a latest-generation land surface model for catchment-scale hydrology at very high spatial resolution. In combination with a meteorological forcing scheme based on multiple in situ stations our model approach strives to ensure internal model consistency and minimize error compensation and equifinality issues (i.e., multiple parameter sets that result in the same "good" performance; e.g., van Tiel et al., 2020), since there is, apart from the adjustment of the elevation above which the precipitation is assumed to be constant, no calibration involved in our study.

However, the mechanistic structure of *T&C* with high spatiotemporal detail is a disadvantage in terms of computational costs, which constrains the spatial and temporal range of the model application and disables long-term simulations for large regions.

Although bulk catchment water balance components can be estimated with conceptual or physically lumped modeling approaches, it is the insight into processes and the detailed water balance partition in the spatiotemporal domain that a process-oriented model like *T&C* provides.

The estimates of evapotranspirative fluxes exemplifies this: the catchment-scale total *ET* (286 mm w.e.; Table 1) simulated in our study for 2019 (wet and cold, based on ERA5-Land climatology 1980–2020; Figure S21 in Supporting Information S1) (286 mm w.e.; Table 1) is comparable to the amount estimated for 2013 (wet and cold; Figure S21 in Supporting Information S1) by Ragettli et al. (2015) using the TOPKAPI-ETH model (228 mm w.e.; Table S6 in Supporting Information S1) and for 1986 (dry and cold; Figure S21 in Supporting Information S1) by Braun et al. (1993) using the HBV3-ETH model (255 mm w.e.; Table S6 in Supporting Information S1). However, those two studies based on either fully conceptual (HBV3-ETH) or simplified process-oriented models (TOPKAPI-ETH), did not include sublimation, so that those estimates overestimate *ET* from soil and vegetation to compensate for the lack of snow sublimation (whose amount we do not know). Hence, catchment water balance estimates, and its single components, can be ill-interpreted and quantified through error compensation or equifinality errors in conceptual and calibrated model approaches.

The physics-based model formulation of *T&C* allows to quantify the processes governing an individual energy or water balance component and enables the determination of which elevation (e.g., Figure 8) and in which subseason (e.g., Figure 7) a particular component contributes to the catchment energy and mass budget. The distributed information ("what," "where," and "when") is not only essential to better constrain the hydrologic functioning of high-elevation catchments, but also to define zones and processes in the catchment that require targeted observations. *T&C*'s ability to reproduce evaporative fluxes has been tested in a number of studies for many land covers and climates (e.g., Botter et al., 2021; Fatichi et al., 2012a; Mastrotheodoros et al., 2020). Because of the scarcity of observations in this part of the world and at high elevations, the evapotranspirative fluxes in our simulations can only be compared to selected point-scale measurements and otherwise needs to be assessed against proxy variables (e.g., surface temperature, soil moisture; Figures 2 and 3).

We investigate within the same modeling framework the joint response of the hydrosphere-cryosphere and biosphere of an HMA catchment. Land surface models have been extensively applied over lowlands and for large domains regionally (e.g., Boone et al., 2009; Mastrotheodoros et al., 2020; Yoon et al., 2019) and globally (e.g., Li et al., 2022), but seldomly to understand the water cycle of high-elevation catchments. Their application to high elevation, complex terrain dominated by snow and ice poses the challenge that the gridded representation of specific meteorological forcing variables is uncertain. Studies on the spatial distribution of wind speed, relative humidity, cloud cover, and incoming shortwave radiation and precipitation would be beneficial to ongoing research for integrated catchment modeling. Whereas vertical temperature lapse rates can be extrapolated toward high altitudes with relative confidence due to a dense network of observations and a clear relationship with elevation, direct measurements to constrain the spatial distribution of precipitation are rare and generally limited to the lower zones of high-elevation catchments (Pritchard, 2021; Winiger et al., 2005). Representing horizontal gradients in precipitation in such catchments would require reasonably high resolution reanalysis or atmospheric simulations (e.g., Collier & Immerzeel, 2015) which remains a future step for this work.

In addition, accurate precipitation measurements have proven extremely difficult to achieve in windy environments (e.g., Liston & Sturm, 2004; Yang et al., 1998). Therefore, there is greater uncertainty in the precipitation in the high elevations of the catchment because of a lack of measurements.

Further, wind is likely higher at high-elevation and wind-exposed sites in complex terrain (e.g., Burlando et al., 2007; as we assumed spatially uniform wind speed, based on the weather station located <4,000 m.a.s.l.), and would therefore increase turbulent heat exchange and likely evaporation and sublimation rates especially from snow and ice. Approaches to account for distributed wind in high mountain environments at the glacier (Bonekamp et al., 2020; Sauter & Galos, 2016), catchment (Vionnet et al., 2014, 2021), and even watershed scale (Peleg et al., 2017) have already been applied and could be considered for a better appraisal of the variability of *ET* in space. Yet, the exact magnitudes of these variations in wind speeds over varying topography cannot be precisely derived nor accurately evaluated. Therefore, there would still remain a degree of uncertainty as to the "real" wind speeds at those mountain peaks are not known, an uncertainty which translates into the overall *ET* calculation.

The knowledge gained from the additional observations described above would pave the way to improve land surface modeling efforts in general, test our findings that vapor fluxes have an important role in catchment hydrology in high-elevation environments, and to examine high-elevation precipitation gradients and distributed precipitation amounts in more detail, ultimately reinforcing the need for mechanistic modeling approaches.

6. Conclusions

We applied a land surface model to gain insight into the detailed partitioning of the water balance in the glacierized Langtang catchment at the subseasonal scale and across elevation bands. The use of a mechanistic, hyper-resolution land surface model allows to shed light on blue-green water fluxes in a high-elevation environment, an emerging focus of research that has been to date neglected in the hydrological analysis of high-elevation, glacierized catchments.

During the hydrological year beginning in 2018, it is evident that the turbulent latent heat flux is an important control of the total water balance, as, in the analyzed period, it causes about the equivalent of 19% of all the available precipitation or 159% of the water production from glacier melt in the basin to return directly to the atmosphere. This water does not contribute to runoff and can in turn affect weather patterns at larger spatial scales through enhanced moisture content in the atmosphere (e.g., de Kok et al., 2018). Partitioning *ET*, snow sublimation is the dominant vapor flux (49% of total *ET*) at the catchment scale, accounting for 11% of snowfall, 17% of snowmelt, and 77% of ice melt, respectively. Evapotranspirative fluxes are particularly important, relative to the other mass fluxes, at both very high and very low elevations. Above 6,500 m.a.s.l., vaporization from snow and ice surfaces is higher than melt. At these elevations, sublimation dictates the depletion of the cryospheric water budget, which instead is snowmelt-dominated at lower elevations. Below 4,500 m.a.s.l., the loss of water through the latent heat flux from soils (evaporation) and vegetation (transpiration) exceeds the input from snowmelt to the water balance. The importance of *ET* increases toward lower elevations with denser vegetation, exceeding the input from rain below 4,000 m.a.s.l., with *ET* from vegetation accounting for 42% of the total evapotranspirative flux in this lowest elevational band. *ET* from vegetation is thus a nonnegligible portion of the water budget (11% of total *ET*; with mostly grass vegetation, whereas shrub and larch account for <1% of the basin), and its importance will increase downstream when considering larger catchment sections or potentially in the future as snow levels recede higher into the mountains.

We remark here that a proper accounting of green water fluxes should be part of catchment hydrology estimates. If models do not consider evapotranspirative fluxes specifically, or derive them as a residual only, catchment water balance estimates can be ill-interpreted and quantified, most likely through error compensations.

The high detail in process representation of our simulations allows us to attribute the relative importance of specific processes. We also quantify two key processes, snow sublimation and *ET* from vegetation, which, in such a catchment, eluded quantification to date.

The Langtang catchment has been extensively studied. Thanks to the efforts of numerous research groups, it has been established as a rather unique monitoring site in HMA, and it has seen a progression of studies that have provided substantial new knowledge on glacier and hydrology of HMA catchments. We have now added to that progression a new step in knowledge, applying a land surface model to provide a revised picture of Langtang's water fluxes and its complex interactions between land and atmosphere. In particular, we have provided for the first time (to our knowledge) catchment-wide estimates of sublimation in HMA, and assessed the role of vegetation in water fluxes partition.

Data Availability Statement

The source code of the *T&C* land surface model is available on GitHub (https://github.com/simonefatichi/TeC_Source_Code) and Code Ocean (https://doi.org/10.24433/CO.0905087.v2). We provide (a) gridded initial conditions, (b) modeled hourly data at the station locations, and (c) monthly gridded outputs for the key simulated variables for the hydrological year 2019 on Zenodo via https://doi.org/10.5281/zenodo.8402426. The ALOS World 3D-30 (AW3D) DEM was released by the Japan Aerospace Exploration Agency (JAXA; Takaku et al., 2014) and downloaded from http://www.opentopography.org. The Pléiades 2017 stereo-pair was provided by the Pléiades Glacier Observatory (PGO) initiative of the French Space Agency (CNES). The Pléiades 2019 stereo-pair was acquired within the scope of the CNES ISIS Programme. Meteorological data are from the regional database of ICIMOD (International Centre for Integrated Mountain Development; http://rds.icimod.org/Home/Data?any=Langtang; Steiner, Gurung, et al., 2021). Shortwave radiation was retrieved from ERA5-Land (Muñoz-Sabater, 2019; Muñoz-Sabater et al., 2021; https://doi.org/10.24381/cds.e2161bac).

T&C was run using the software MATLAB version 2016b (Mathworks, 2016) on the WSL-Hyperion cluster (Birmensdorf, Switzerland). Topographical preprocessing steps were performed using Topotoolbox (Schwanghart and Scherler, 2014) and the Upslope area functions (Eddins, 2022) with the software MATLAB version 2021b (Mathworks, 2021). All postprocessing analysis was done using the R language and software (R Core Team, 2020; RStudio Team, 2022).

References

Ageta, Y., & Higuchi, K. (1984). Estimation of mass balance components of a summer-accumulation type glacier in the Nepal Himalaya. *Geografiska Annaler-Series A: Physical Geography*, *66*(3), 249–255. https://doi.org/10.1080/04353676.1984.11880113

Anderson, L. S., & Anderson, R. S. (2018). Debris thickness patterns on debris-covered glaciers. *Geomorphology*, *311*, 1–12. https://doi.org/10.1016/j.geomorph.2018.03.014

Arora, V. K., & Boer, G. J. (2005). A parameterization of leaf phenology for the terrestrial ecosystem component of climate models. *Global Change Biology*, *11*(1), 39–59. https://doi.org/10.1111/j.1365-2486.2004.00890.x

Azam, M. F., Kargel, J. S., Shea, J. M., Nepal, S., Haritashya, U. K., Srivastava, S., et al. (2021). Glaciohydrology of the Himalaya-Karakoram. *Science*, *373*(6557), eabf3668. https://doi.org/10.1126/science.abf3668

Bandyopadhyay, J., Kraemer, D., Kattelmann, R., & Kundzewicz, Z. W. (1997). Highland waters: A resource of global significance. In B. Messerli, & J. Ives (Eds.), *Mountains of the world: A global priority* (pp. 131–155). Parthenon.

Bernhardt, M., & Schulz, K. (2010). SnowSlide: A simple routine for calculating gravitational snow transport. *Geophysical Research Letters*, *37*, L11502. https://doi.org/10.1029/2010GL043086

Beug, H. J., & Miehe, G. (1999). Vegetation history and human impact in the Eastern Central-Himalaya (Langtang and Helambu, Nepal). *Dissertaciones Botanicae*, *318*, 98.

Biemans, H., Siderius, C., Lutz, A. F., Nepal, S., Ahmad, B., Hassan, T., et al. (2019). Importance of snow and glacier meltwater for agriculture on the Indo-Gangetic Plain. *Nature Sustainability*, *2*(7), 594–601. https://doi.org/10.1038/s41893-019-0305-3

Bonekamp, P. N. J., Collier, E., & Immerzeel, W. W. (2018). The impact of spatial resolution, land use, and spinup time on resolving spatial precipitation patterns in the Himalayas. *Journal of Hydrometeorology*, *19*(10), 1565–1581. https://doi.org/10.1175/jhm-d-17-0212.1

Bonekamp, P. N. J., Van Heerwaarden, C. C., Steiner, J. F., & Immerzeel, W. W. (2020). Using 3D turbulence-resolving simulations to understand the impact of surface properties on the energy balance of a debris-covered glacier. *The Cryosphere*, *14*(5), 1611–1632. https://doi.org/10.5194/tc-14-1611-2020

Boone, A., De Rosnay, P., Balsamo, G., Beljaars, A., Chopin, F., Decharme, B., et al. (2009). The AMMA land surface model intercomparison project (ALMIP). *Bulletin of the American Meteorological Society*, *90*(12), 1865–1880. https://doi.org/10.1175/2009bams2786.1

Botter, M., Zeeman, M., Burlando, P., & Fatichi, S. (2021). Impacts of fertilization on grassland productivity and water quality across the European Alps under current and warming climate: Insights from a mechanistic model. *Biogeosciences*, *18*(6), 1917–1939. https://doi.org/10.5194/bg-2020-294

Braun, L. N., Grabs, W., & Rana, B. (1993). Application of a conceptual precipitation-runoff model in the Langtang Khola basin, Nepal Himalaya. *IAHS Publication*, *218*, 221–238.

Broxton, P. D., Harpold, A. A., Biederman, J. A., Troch, P. A., Molotch, N. P., & Brooks, P. D. (2015). Quantifying the effects of vegetation structure on snow accumulation and ablation in mixed-conifer forests. *Ecohydrology*, *8*(6), 1073–1094. https://doi.org/10.1002/eco.1565

Brun, F., Berthier, E., Wagnon, P., Kääb, A., & Treichler, D. (2017). A spatially resolved estimate of High Mountain Asia glacier mass balances from 2000 to 2016. *Nature Geoscience*, *10*(9), 668–673. https://doi.org/10.1038/ngeo2999

Brutsaert, W. (2005). *Hydrology: An introduction*. Cambridge University Press.

Brutsaert, W. (1982). *Evaporation into the atmosphere*. D. Reidel.

Buchhorn, M., Smets, B., Bertels, L., Lesiv, M., Tsendbazar, N.-E., Masiliunas, D., et al. (2020). Copernicus global land Service: Land cover 100m: Collection 3: Epoch 2019: Globe (version V3.0.1) [Dataset]. Zenodo. https://doi.org/10.5281/zenodo.3939050

Buri, P., Miles, E. S., Steiner, J. F., Ragettli, S., & Pellicciotti, F. (2021). Supraglacial ice cliffs can substantially increase the mass loss of debris-covered glaciers. *Geophysical Research Letters*, *48*, e2020GL092150. https://doi.org/10.1029/2020GL092150

Burlando, M., Carassale, L., Georgieva, E., Ratto, C. F., & Solari, G. (2007). A simple and efficient procedure for the numerical simulation of wind fields in complex terrain. *Boundary-Layer Meteorology*, *125*(3), 417–439. https://doi.org/10.1007/s10546-007-9196-3

Chang, Y., Wang, J., Qin, D., Ding, Y., Zhao, Q., Liu, F., & Zhang, S. (2017). Methodological comparison of alpine meadow evapotranspiration on the Tibetan Plateau, China. *PLoS One*, *12*(12), e0189059. https://doi.org/10.1371/journal.pone.0189059

Chen, X., Su, Z., Ma, Y., Liu, S., Yu, Q., & Xu, Z. (2014). Development of a 10-year (2001–2010) 0.1° data set of land-surface energy balance for mainland China. *Atmospheric Chemistry and Physics*, *14*(23), 13097–13117. https://doi.org/10.5194/acp-14-13097-2014

Collier, E., & Immerzeel, W. W. (2015). High-resolution modeling of atmospheric dynamics in the Nepalese Himalaya. *Journal of Geophysical Research: Atmospheres*, *120*, 9882–9896. https://doi.org/10.1002/2015JD023266

Daly, C., Neilson, R. P., & Phillips, D. L. (1994). A statistical-topographic model for mapping climatological precipitation over mountainous terrain. *Journal of Applied Meteorology and Climatology*, *33*(2), 140–158. https://doi.org/10.1175/1520-0450(1994)033<0140:astmfm>2.0.co;2

de Kok, R. J., Tuinenburg, O. A., Bonekamp, P. N., & Immerzeel, W. W. (2018). Irrigation as a potential driver for anomalous glacier behavior in High Mountain Asia. *Geophysical Research Letters*, *45*, 2047–2054. https://doi.org/10.1002/2017GL076158

Ding, B., Yang, K., Qin, J., Wang, L., Chen, Y., & He, X. (2014). The dependence of precipitation types on surface elevation and meteorological conditions and its parameterization. *Journal of Hydrology*, *513*, 154–163. https://doi.org/10.1016/j.jhydrol.2014.03.038

Ding, B., Yang, K., Yang, W., He, X., Chen, Y., Lazhu, et al. (2017). Development of a Water and Enthalpy Budget-based Glacier mass balance Model (WEB-GM) and its preliminary validation. *Water Resources Research*, *53*, 3146–3178. https://doi.org/10.1002/2016WR018865

Duethmann, D., Menz, C., Jiang, T., & Vorogushyn, S. (2016). Projections for headwater catchments of the Tarim River reveal glacier retreat and decreasing surface water availability but uncertainties are large. *Environmental Research Letters*, *11*(5), 054024. https://doi.org/10.1088/1748-9326/11/5/054024

Eddins, S. (2022). Upslope area functions. In *MATLAB Central File Exchange*. Retrieved from https://www.mathworks.com/matlabcentral/fileexchange/15818-upslope-area-functions

Farinotti, D., Huss, M., Fürst, J. J., Landmann, J., Machguth, H., Maussion, F., & Pandit, A. (2019). A consensus estimate for the ice thickness distribution of all glaciers on Earth. *Nature Geoscience*, *12*(3), 168–173. https://doi.org/10.1038/s41561-019-0300-3

Fatichi, S., Ivanov, V. Y., & Caporali, E. (2012a). A mechanistic ecohydrological model to investigate complex interactions in cold and warm water-controlled environments: 1. Theoretical framework and plot-scale analysis. *Journal of Advances in Modeling Earth Systems*, *4*, M05002. https://doi.org/10.1029/2011MS000086

Fatichi, S., Ivanov, V. Y., & Caporali, E. (2012b). A mechanistic ecohydrological model to investigate complex interactions in cold and warm water-controlled environments: 2. Spatiotemporal analyses. *Journal of Advances in Modeling Earth Systems*, *4*, M05003. https://doi.org/10.1029/2011MS000087

Fatichi, S., Peleg, N., Mastrotheodoros, T., Pappas, C., & Manoli, G. (2021). An ecohydrological journey of 4500 years reveals a stable but threatened precipitation-groundwater recharge relation around Jerusalem. *Science Advances*, *7*(37), eabe6303. https://doi.org/10.1126/sciadv.abe6303

Fatichi, S., Vivoni, E. R., Ogden, F. L., Ivanov, V. Y., Mirus, B., Gochis, D., et al. (2016). An overview of current applications, challenges, and future trends in distributed process-based models in hydrology. *Journal of Hydrology*, *537*, 45–60. https://doi.org/10.1016/j.jhydrol.2016.03.026

Fisher, J. B., Lee, B., Purdy, A. J., Halverson, G. H., Dohlen, M. B., Cawse-Nicholson, K., et al. (2020). Ecostress: NASA's next generation mission to measure evapotranspiration from the international space station. *Water Resources Research*, *56*, e2019WR026058. https://doi.org/10.1029/2019WR026058

Fugger, S., Fyffe, C. L., Fatichi, S., Miles, E., McCarthy, M., Shaw, T. E., et al. (2022). Understanding monsoon controls on the energy and mass balance of glaciers in the Central and Eastern Himalaya. *The Cryosphere*, *16*(5), 1631–1652. https://doi.org/10.5194/tc-16-1631-2022

Fujita, K. (2008). Effect of precipitation seasonality on climatic sensitivity of glacier mass balance. *Earth and Planetary Science Letters*, *276*(1–2), 14–19. https://doi.org/10.1016/j.epsl.2008.08.028

Fujita, K., & Sakai, A. (2014). Modelling runoff from a Himalayan debris-covered glacier. *Hydrology and Earth System Sciences*, *18*(7), 2679–2694. https://doi.org/10.5194/hess-18-2679-2014

Fujita, K., Sakai, A., & Chhetri, T. B. (1997). Meteorological observation in Langtang Valley, Nepal Himalayas, 1996. *Bulletin of Glacier Research*, *15*, 71–78.

Fujita, K., Takeuchi, N., & Seko, K. (1998). Glaciological observations of Yala Glacier in Langtang Valley, Nepal Himalayas, 1994 and. *Bulletin of Glacier Research*, *16*, 75–78.

Fukushima, Y. (1991). Estimation of streamflow change by global warming in a glacier-covered high mountain area of the Nepal Himalaya. In *Proceedings of the Vienna symposium, August 1991* (Vol. 205, pp, 181–188). IAHS Publication.

Fyffe, C. L., Potter, E., Fugger, S., Orr, A., Fatichi, S., Loarte, E., et al. (2021). The energy and mass balance of Peruvian glaciers. *Journal of Geophysical Research: Atmospheres*, *126*, e2021JD034911. https://doi.org/10.1029/2021JD034911

Garratt, J. R. (1992). *The atmospheric boundary layer.* Cambridge University Press.

Gascoin, S. (2021). Snowmelt and snow sublimation in the Indus basin. *Water*, *13*(19), 2621. https://doi.org/10.3390/w13192621

Girona-Mata, M., Miles, E. S., Ragettli, S., & Pellicciotti, F. (2019). High-resolution snowline delineation from Landsat imagery to infer snow cover controls in a Himalayan catchment. *Water Resources Research*, *55*, 6754–6772. https://doi.org/10.1029/2019WR024935

Günther, D., Marke, T., Essery, R., & Strasser, U. (2019). Uncertainties in snowpack simulations-assessing the impact of model structure, parameter choice, and forcing data error on point-scale energy balance snow model performance. *Water Resources Research*, *55*, 2779–2800. https://doi.org/10.1029/2018WR023403

He, S., Zhang, Y., Ma, N., Tian, J., Kong, D., & Liu, C. (2022). A daily and 500 m coupled evapotranspiration and gross primary production product across China during 2000–2020. *Earth System Science Data*, *14*(12), 5463–5488.

Heynen, M., Miles, E., Ragettli, S., Buri, P., Immerzeel, W. W., & Pellicciotti, F. (2016). Air temperature variability in a high-elevation Himalayan catchment. *Annals of Glaciology*, *57*(71), 212–222. https://doi.org/10.3189/2016aog71a076

Higuchi, K. (Ed.), (1984). *Glacial studies in Langtang Valley: Report of the glacier boring project 1981–82 in the Nepal Himalaya.* Data Center for Glacier Research, Japanese Society of Snow and Ice.

Hopp, L., Fatichi, S., & Ivanov, V. Y. (2016). Simulating water flow in variably saturated soils: A comparison of a 3-D model with approximation-based formulations. *Hydrology Research*, *47*(2), 274–290. https://doi.org/10.2166/nh.2015.126

Hugonnet, R., McNabb, R., Berthier, E., Menounos, B., Nuth, C., Girod, L., et al. (2021). Accelerated global glacier mass loss in the early twenty-first century. *Nature*, *592*(7856), 726–731. https://doi.org/10.1038/s41586-021-03436-z

Hulley, G. C., Göttsche, F. M., Rivera, G., Hook, S. J., Freepartner, R. J., Martin, M. A., et al. (2021). Validation and quality assessment of the ECOSTRESS level-2 land surface temperature and emissivity product. *IEEE Transactions on Geoscience and Remote Sensing*, *60*, 1–23. https://doi.org/10.1109/tgrs.2021.3079879

Huss, M., & Hock, R. (2018). Global-scale hydrological response to future glacier mass loss. *Nature Climate Change*, *8*(2), 135–140. https://doi.org/10.1038/s41558-017-0049-x

ICIMOD. (2016a). Meteorological data from Kyanging automatic weather station [Dataset]. ICIMOD. https://doi.org/10.26066/RDS.22464

ICIMOD. (2016b). Meteorological data from Yala Base Camp automatic weather station [Dataset]. ICIMOD. https://doi.org/10.26066/RDS.26859

Immerzeel, W. W., Lutz, A. F., Andrade, M., Bahl, A., Biemans, H., Bolch, T., et al. (2020). Importance and vulnerability of the world's water towers. *Nature*, *577*(7790), 364–369. https://doi.org/10.1038/s41586-019-1822-y

Immerzeel, W. W., Pellicciotti, F., & Bierkens, M. F. P. (2013). Rising river flows throughout the twenty-first century in two Himalayan glacierized watersheds. *Nature Geoscience*, *6*(9), 742–745. https://doi.org/10.1038/ngeo1896

Immerzeel, W. W., Pellicciotti, F., & Shrestha, A. B. (2012). Glaciers as a proxy to quantify the spatial distribution of precipitation in the Hunza basin. *Mountain Research and Development*, *32*(1), 30–38. https://doi.org/10.1659/mrd-journal-d-11-00097.1

Immerzeel, W. W., Petersen, L., Ragettli, S., & Pellicciotti, F. (2014). The importance of observed gradients of air temperature and precipitation for modeling runoff from a glacierized watershed in the Nepalese Himalayas. *Water Resources Research*, *50*, 2212–2226. https://doi.org/10.1002/2013WR014506

Immerzeel, W. W., Van Beek, L. P., & Bierkens, M. F. (2010). Climate change will affect the Asian water towers. *Science*, *328*(5984), 1382–1385. https://doi.org/10.1126/science.1183188

Immerzeel, W. W., Van Beek, L. P. H., Konz, M., Shrestha, A. B., & Bierkens, M. F. P. (2012). Hydrological response to climate change in a glacierized catchment in the Himalayas. *Climatic Change*, *110*(3), 721–736. https://doi.org/10.1007/s10584-011-0143-4

Jouberton, A., Shaw, T. E., Miles, E., McCarthy, M., Fugger, S., Ren, S., et al. (2022). Warming-induced monsoon precipitation phase change intensifies glacier mass loss in the southeastern Tibetan Plateau. *Proceedings of the National Academy of Sciences of the United States of America*, *119*(37), e2109796119. https://doi.org/10.1073/pnas.2109796119

Jung, M., Koirala, S., Weber, U., Ichii, K., Gans, F., Camps-Valls, G., et al. (2019). The FLUXCOM ensemble of global land-atmosphere energy fluxes. *Scientific Data*, *6*(1), 74. https://doi.org/10.1038/s41597-019-0076-8

Khadka, M., Kayastha, R. B., & Kayastha, R. (2020). Future projection of cryospheric and hydrologic regimes in Koshi River basin, Central Himalaya, using coupled glacier dynamics and glacio-hydrological models. *Journal of Glaciology*, *66*(259), 831–845. https://doi.org/10.1017/jog.2020.51

Kneib, M., Fyffe, C. L., Miles, E. S., Lindemann, S., Shaw, T. E., Buri, P., et al. (2023). Controls on ice cliff distribution and characteristics on debris-covered glaciers. *Geophysical Research Letters*, *50*, e2022GL102444. https://doi.org/10.1029/2022GL102444

Kneib, M., Miles, E. S., Buri, P., Molnar, P., McCarthy, M., Fugger, S., & Pellicciotti, F. (2021). Interannual dynamics of ice cliff populations on debris-covered glaciers from remote sensing observations and stochastic modeling. *Journal of Geophysical Research: Earth Surface*, *126*, e2021JF006179. https://doi.org/10.1029/2021JF006179

Kneib, M., Miles, E. S., Jola, S., Buri, P., Herreid, S., Bhattacharya, A., et al. (2021). Mapping ice cliffs on debris-covered glaciers using multispectral satellite images. *Remote Sensing of Environment*, *253*, 112201. https://doi.org/10.1016/j.rse.2020.112201

Konz, M., Uhlenbrook, S., Braun, L., Shrestha, A., & Demuth, S. (2007). Implementation of a process-based catchment model in a poorly gauged, highly glacierized Himalayan headwater. *Hydrology and Earth System Sciences*, *11*(4), 1323–1339. https://doi.org/10.5194/hess-11-1323-2007

Lau, W. K., Kim, M. K., Kim, K. M., & Lee, W. S. (2010). Enhanced surface warming and accelerated snow melt in the Himalayas and Tibetan Plateau induced by absorbing aerosols. *Environmental Research Letters*, *5*(2), 025204. https://doi.org/10.1088/1748-9326/5/2/025204

Li, J., Miao, C., Zhang, G., Fang, Y. H., Shangguan, W., & Niu, G. Y. (2022). Global evaluation of the Noah-MP land surface model and suggestions for selecting parameterization schemes. *Journal of Geophysical Research: Atmospheres*, *127*, e2021JD035753. https://doi.org/10.1029/2021JD035753

Liston, G. E., & Sturm, M. (2004). The role of winter sublimation in the Arctic moisture budget. *Hydrology Research*, *35*(4–5), 325–334. https://doi.org/10.2166/nh.2004.0024

Lu, J., Wang, G., Chen, T., Li, S., Hagan, D. F. T., Kattel, G., et al. (2021). A harmonized global land evaporation dataset from model-based products covering 1980–2017. *Earth System Science Data*, *13*(12), 5879–5898. https://doi.org/10.5194/essd-13-5879-2021

Lutz, A. F., Immerzeel, W. W., Shrestha, A. B., & Bierkens, M. F. P. (2014). Consistent increase in high Asia's runoff due to increasing glacier melt and precipitation. *Nature Climate Change*, *4*(7), 587–592. https://doi.org/10.1038/nclimate2237

MacDonald, M. K., Pomeroy, J. W., & Pietroniro, A. (2010). On the importance of sublimation to an alpine snow mass balance in the Canadian Rocky Mountains. *Hydrology and Earth System Sciences*, *14*(7), 1401–1415. https://doi.org/10.5194/hess-14-1401-2010

Mandal, A., Angchuk, T., Azam, M. F., Ramanathan, A., Wagnon, P., Soheb, M., & Singh, C. (2022). An 11-year record of wintertime snow-surface energy balance and sublimation at 4863 m a.s.l. on the Chhota Shigri Glacier moraine (western Himalaya, India). *The Cryosphere*, *16*(9), 3775–3799. https://doi.org/10.5194/tc-16-3775-2022

Martens, B., Miralles, D. G., Lievens, H., Van Der Schalie, R., De Jeu, R. A., Fernández-Prieto, D., et al. (2017). GLEAM v3: Satellite-based land evaporation and root-zone soil moisture. *Geoscientific Model Development*, *10*(5), 1903–1925. https://doi.org/10.5194/gmd-10-1903-2017

Marty, C., Philipona, R., Fröhlich, C., & Ohmura, A. (2002). Altitude dependence of surface radiation fluxes and cloud forcing in the alps: Results from the alpine surface radiation budget network. *Theoretical and Applied Climatology*, *72*(3), 137–155. https://doi.org/10.1007/s007040200019

Mascart, P., Noilhan, J., & Giordani, H. (1995). A modified parameterization of flux-profile relationships in the surface layer using different roughness length values for heat and momentum. *Boundary-Layer Meteorology*, *72*(4), 331–344. https://doi.org/10.1007/bf00708998

Mastrotheodoros, T., Pappas, C., Molnar, P., Burlando, P., Hadjidoukas, P., & Fatichi, S. (2019). Ecohydrological dynamics in the Alps: Insights from a modelling analysis of the spatial variability. *Ecohydrology*, *12*(1), e2054. https://doi.org/10.1002/eco.2054

Mastrotheodoros, T., Pappas, C., Molnar, P., Burlando, P., Manoli, G., Parajka, J., et al. (2020). More green and less blue water in the Alps during warmer summers. *Nature Climate Change*, *10*(2), 155–161. https://doi.org/10.1038/s41558-019-0676-5

Mathworks. (2016). *Mathworks, Inc. MATLAB. Version 2016b. Computer software*. Mathworks, Inc. Retrieved from www.mathworks.com/

Mathworks. (2021). *Mathworks, Inc. MATLAB. Version 2021b. Computer software*. Mathworks, Inc. Retrieved from www.mathworks.com/

Maurer, J. M., Schaefer, J. M., Rupper, S., & Corley, A. J. S. A. (2019). Acceleration of ice loss across the Himalayas over the past 40 years. *Science Advances*, *5*(6), eaav7266. https://doi.org/10.1126/sciadv.aav7266

McCarthy, M., Miles, E., Kneib, M., Buri, P., Fugger, S., & Pellicciotti, F. (2022). Supraglacial debris thickness and supply rate in High-Mountain Asia. *Communications Earth & Environment*, *3*(1), 269. https://doi.org/10.1038/s43247-022-00588-2

McCarthy, M., Pritchard, H., Willis, I. A. N., & King, E. (2017). Ground-penetrating radar measurements of debris thickness on Lirung Glacier, Nepal. *Journal of Glaciology*, *63*(239), 543–555. https://doi.org/10.1017/jog.2017.18

McDowell, G., Koppes, M., Harris, L., Chan, K. M., Price, M. F., Lama, D. G., & Jiménez, G. (2022). Lived experiences of 'peak water' in the high mountains of Nepal and Peru. *Climate & Development*, *14*(3), 268–281. https://doi.org/10.1080/17565529.2021.1913085

Miles, E., McCarthy, M., Dehecq, A., Kneib, M., Fugger, S., & Pellicciotti, F. (2021). Health and sustainability of glaciers in High Mountain Asia. *Nature Communications*, *12*(1), 2868. https://doi.org/10.1038/s41467-021-23073-4

Miles, E. S., Willis, I., Buri, P., Steiner, J. F., Arnold, N. S., & Pellicciotti, F. (2018). Surface pond energy absorption across four Himalayan glaciers accounts for 1/8 of total catchment ice loss. *Geophysical Research Letters*, *45*, 10464–10473. https://doi.org/10.1029/2018GL079678

Miles, E. S., Willis, I. C., Arnold, N. S., Steiner, J., & Pellicciotti, F. (2017). Spatial, seasonal and interannual variability of supraglacial ponds in the Langtang Valley of Nepal, 1999–2013. *Journal of Glaciology*, *63*(237), 88–105. https://doi.org/10.1017/jog.2016.120

Mimeau, L., Esteves, M., Zin, I., Jacobi, H. W., Brun, F., Wagnon, P., et al. (2019). Quantification of different flow components in a high-altitude glacierized catchment (Dudh Koshi, Himalaya): Some cryospheric-related issues. *Hydrology and Earth System Sciences*, *23*(9), 3969–3996. https://doi.org/10.5194/hess-23-3969-2019

Morinaga, Y., Seko, K., & Takahashi, S. (1987). Seasonal variation of snowline in Langtang Valley, Nepal Himalayas, 1985–1986. *Bulletin of Glacier Research*, *5*, 49–53.

Mu, Q., Zhao, M., & Running, S. W. (2011). Improvements to a MODIS global terrestrial evapotranspiration algorithm. *Remote Sensing of Environment*, *115*(8), 1781–1800. https://doi.org/10.1016/j.rse.2011.02.019

Muñoz-Sabater, J. (2019). *ERA5-Land hourly data from 1981 to present*. Copernicus Climate Change Service (C3S) Climate Data Store (CDS). https://doi.org/10.24381/cds.e2161bac

Muñoz-Sabater, J., Dutra, E., Agustí-Panareda, A., Albergel, C., Arduini, G., Balsamo, G., et al. (2021). ERA5-Land: A state-of-the-art global reanalysis dataset for land applications. *Earth System Science Data*, *13*(9), 4349–4383. https://doi.org/10.5194/essd-13-4349-2021

Nie, Y., Pritchard, H. D., Liu, Q., Hennig, T., Wang, W., Wang, X., et al. (2021). Glacial change and hydrological implications in the Himalaya and Karakoram. *Nature Reviews Earth & Environment*, *2*(2), 91–106. https://doi.org/10.1038/s43017-020-00124-w

Núñez, C. M., Varas, E. A., & Meza, F. J. (2010). Modelling soil heat flux. *Theoretical and Applied Climatology*, *100*(3–4), 251–260. https://doi.org/10.1007/s00704-009-0185-y

Parajka, J., & Blöschl, G. (2008). Spatio-temporal combination of MODIS images—Potential for snow cover mapping. *Water Resources Research*, *44*, W03406. https://doi.org/10.1029/2007WR006204

Paschalis, A., Fatichi, S., Pappas, C., & Or, D. (2018). Covariation of vegetation and climate constraints present and future T/ET variability. *Environmental Research Letters*, *13*(10), 104012. https://doi.org/10.1088/1748-9326/aae267

Peleg, N., Fatichi, S., Paschalis, A., Molnar, P., & Burlando, P. (2017). An advanced stochastic weather generator for simulating 2-D high-resolution climate variables. *Journal of Advances in Modeling Earth Systems*, *9*, 1595–1627. https://doi.org/10.1002/2016MS000854

Pellicciotti, F., Stephan, C., Miles, E., Herreid, S., Immerzeel, W. W., & Bolch, T. (2015). Mass-balance changes of the debris-covered glaciers in the Langtang Himal, Nepal, from 1974 to 1999. *Journal of Glaciology*, *61*(226), 373–386. https://doi.org/10.3189/2015jog13j237

Poggio, L., de Sousa, L. M., Batjes, N. H., Heuvelink, G. B. M., Kempen, B., Ribeiro, E., & Rossiter, D. (2021). SoilGrids 2.0: Producing soil information for the globe with quantified spatial uncertainty. *SOIL*, *7*(1), 217–240. https://doi.org/10.5194/soil-7-217-2021

Pohl, E., Gloaguen, R., Andermann, C., & Knoche, M. (2017). Glacier melt buffers river runoff in the Pamir Mountains. *Water Resources Research*, *53*, 2467–2489. https://doi.org/10.1002/2016WR019431

Pohl, E., Knoche, M., Gloaguen, R., Andermann, C., & Krause, P. (2015). Sensitivity analysis and implications for surface processes from a hydrological modelling approach in the Gunt catchment, high Pamir Mountains. *Earth Surface Dynamics*, *3*(3), 333–362. https://doi.org/10.5194/esurf-3-333-2015

Pomeroy, J. W., Parviainen, J., Hedstrom, N., & Gray, D. M. (1998). Coupled modelling of forest snow interception and sublimation. *Hydrological Processes*, *12*(15), 2317–2337. https://doi.org/10.1002/(sici)1099-1085(199812)12:15<2317::aid-hyp799>3.0.co;2-x

Pradhananga, D., & Pomeroy, J. W. (2022). Diagnosing changes in glacier hydrology from physical principles using a hydrological model with snow redistribution, sublimation, firnification and energy balance ablation algorithms. *Journal of Hydrology*, *608*, 127545. https://doi.org/10.1016/j.jhydrol.2022.127545

Pritchard, H. D. (2019). Asia's shrinking glaciers protect large populations from drought stress. *Nature*, *569*(7758), 649–654. https://doi.org/10.1038/s41586-019-1240-1

Pritchard, H. D. (2021). Global data gaps in our knowledge of the terrestrial cryosphere. *Frontiers in Climate*, *3*, 689823. https://doi.org/10.3389/fclim.2021.689823

Racoviteanu, A. E., Armstrong, R., & Williams, M. W. (2013). Evaluation of an ice ablation model to estimate the contribution of melting glacier ice to annual discharge in the Nepal Himalaya. *Water Resources Research*, *49*, 5117–5133. https://doi.org/10.1002/wrcr.20370

Ragettli, S., Bolch, T., & Pellicciotti, F. (2016). Heterogeneous glacier thinning patterns over the last 40 years in Langtang Himal, Nepal. *The Cryosphere*, *10*(5), 2075–2097. https://doi.org/10.5194/tc-10-2075-2016

Ragettli, S., Immerzeel, W. W., & Pellicciotti, F. (2016). Contrasting climate change impact on river flows from high-altitude catchments in the Himalayan and Andes Mountains. *Proceedings of the National Academy of Sciences of the United States of America*, *113*(33), 9222–9227. https://doi.org/10.1073/pnas.1606526113

Ragettli, S., Pellicciotti, F., Immerzeel, W. W., Miles, E. S., Petersen, L., Heynen, M., et al. (2015). Unraveling the hydrology of a Himalayan catchment through integration of high resolution in situ data and remote sensing with an advanced simulation model. *Advances in Water Resources*, *78*, 94–111. https://doi.org/10.1016/j.advwatres.2015.01.013

R Core Team. (2020). *R: A language and environment for statistical computing*. R Foundation for Statistical Computing. Retrieved from https://www.R-project.org/

Reba, M. L., Pomeroy, J., Marks, D., & Link, T. E. (2012). Estimating surface sublimation losses from snowpacks in a mountain catchment using eddy covariance and turbulent transfer calculations. *Hydrological Processes*, *26*(24), 3699–3711. https://doi.org/10.1002/hyp.8372

Reid, T. D., & Brock, B. W. (2010). An energy-balance model for debris-covered glaciers including heat conduction through the debris layer. *Journal of Glaciology*, *56*(199), 903–916. https://doi.org/10.3189/002214310794457218

Ren, S., Miles, E. S., Jia, L., Menenti, M., Kneib, M., Buri, P., et al. (2021). Anisotropy parameterization development and evaluation for glacier surface albedo retrieval from satellite observations. *Remote Sensing*, *13*(9), 1714. https://doi.org/10.3390/rs13091714

RGI Consortium. (2017). *Randolph Glacier Inventory—A dataset of global glacier outlines, version 6*. NSIDC: National Snow and Ice Data Center. https://doi.org/10.7265/4m1f-gd79

Rouholahnejad Freund, E., & Kirchner, J. W. (2017). A Budyko framework for estimating how spatial heterogeneity and lateral moisture redistribution affect average evapotranspiration rates as seen from the atmosphere. *Hydrology and Earth System Sciences*, *21*(1), 217–233. https://doi.org/10.5194/hess-21-217-2017

Rowan, A. V., Egholm, D. L., Quincey, D. J., & Glasser, N. F. (2015). Modelling the feedbacks between mass balance, ice flow and debris transport to predict the response to climate change of debris-covered glaciers in the Himalaya. *Earth and Planetary Science Letters*, *430*, 427–438. https://doi.org/10.1016/j.epsl.2015.09.004

RStudio Team. (2022). *RStudio*. Integrated Development Environment for R. RStudio, PBC. Retrieved from http://www.rstudio.com/

Sauter, T., & Galos, S. P. (2016). Effects of local advection on the spatial sensible heat flux variation on a mountain glacier. *The Cryosphere*, *10*(6), 2887–2905. https://doi.org/10.5194/tc-10-2887-2016

Saxton, K. E., & Rawls, W. J. (2006). Soil water characteristic estimates by texture and organic matter for hydrologic solutions. *Soil Science Society of America Journal*, *70*(5), 1569–1578. https://doi.org/10.2136/sssaj2005.0117

Scherler, D., Wulf, H., & Gorelick, N. (2018). Global assessment of supraglacial debris-cover extents. *Geophysical Research Letters*, *45*, 11798–11805. https://doi.org/10.1029/2018GL080158

Schmitz, M., & Sourell, H. (2000). Variability in soil moisture measurements. *Irrigation Science*, *19*(3), 147–151. https://doi.org/10.1007/s002710000015

Schwanghart, W., & Scherler, D. (2014). TopoToolbox 2—MATLAB-based software for topographic analysis and modeling in Earth surface sciences. *Earth Surface Dynamics*, *2*(1), 1–7. https://doi.org/10.5194/esurf-2-1-2014

Seko, K. (1987). Seasonal variation of altitudinal dependence of precipitation in Langtang Valley, Nepal Himalayas. *Bulletin of Glacier Research*, *5*, 41–47.

Seko, K., & Takahashi, S. (1991). Characteristics of winter precipitation and its effect on glaciers in the Nepal Himalaya. *Bulletin of Glacier Research*, *9*, 9–16.

Shaw, T. E., Miles, E. S., Chen, D., Jouberton, A., Kneib, M., Fugger, S., et al. (2022). Multi-decadal monsoon characteristics and glacier response in High Mountain Asia. *Environmental Research Letters*, *17*(10), 104001. https://doi.org/10.1088/1748-9326/ac9008

Shaw, T. E., Yang, W., Ayala, Á., Bravo, C., Zhao, C., & Pellicciotti, F. (2021). Distributed summer air temperatures across mountain glaciers in the south-east Tibetan Plateau: Temperature sensitivity and comparison with existing glacier datasets. *The Cryosphere*, *15*(2), 595–614. https://doi.org/10.5194/tc-15-595-2021

Shea, J. M., & Moore, R. D. (2010). Prediction of spatially distributed regional-scale fields of air temperature and vapor pressure over mountain glaciers. *Journal of Geophysical Research*, *115*, D23107. https://doi.org/10.1029/2010JD014351

Shean, D. E., Bhushan, S., Montesano, P., Rounce, D. R., Arendt, A., & Osmanoglu, B. (2020). A systematic, regional assessment of High Mountain Asia glacier mass balance. *Frontiers in Earth Science*, *7*, 363. https://doi.org/10.3389/feart.2019.00363

Sherpa, T. C., Matthews, T., Perry, L. B., Thapa, A., Singh, P. K., Khadka, A., et al. (2023). Insights from the first winter weather observations near Mount Everest's summit. *Weather*. https://doi.org/10.1002/wea.4374

Sorg, A., Huss, M., Rohrer, M., & Stoffel, M. (2014). The days of plenty might soon be over in glacierized Central Asian catchments. *Environmental Research Letters*, *9*(10), 104018. https://doi.org/10.1088/1748-9326/9/10/104018

Steiner, J. F., Buri, P., Miles, E. S., Ragettli, S., & Pellicciotti, F. (2019). Supraglacial ice cliffs and ponds on debris-covered glaciers: Spatio-temporal distribution and characteristics. *Journal of Glaciology*, *65*(252), 617–632. https://doi.org/10.1017/jog.2019.40

Steiner, J. F., Gurung, T. R., Joshi, S. P., Koch, I., Saloranta, T., Shea, J., et al. (2021). Multi-year observations of the high mountain water cycle in the Langtang catchment, Central Himalaya. *Hydrological Processes*, *35*(5), e14189. https://doi.org/10.1002/hyp.14189

Steiner, J. F., Kraaijenbrink, P. D., & Immerzeel, W. W. (2021a). Distributed melt on a debris-covered glacier: Field observations and melt modeling on the Lirung Glacier in the Himalaya. *Frontiers in Earth Science*, *9*, 678375. https://doi.org/10.3389/feart.2021.678375

Stigter, E. E., Litt, M., Steiner, J. F., Bonekamp, P. N., Shea, J. M., Bierkens, M. F., & Immerzeel, W. W. (2018). The importance of snow sublimation on a Himalayan glacier. *Frontiers in Earth Science*, *6*, 108. https://doi.org/10.3389/feart.2018.00108

Strasser, U., Bernhardt, M., Weber, M., Liston, G. E., & Mauser, W. (2008). Is snow sublimation important in the alpine water balance? *The Cryosphere*, *2*(1), 53–66. https://doi.org/10.5194/tc-2-53-2008

Takaku, J., Tadono, T., & Tsutsui, K. (2014). Generation of high resolution global DSM from ALOS PRISM. *ISPRS Annals of Photogrammetry, Remote Sensing & Spatial Information Sciences*, *2*(4), 243–248. https://doi.org/10.5194/isprsarchives-XL-4-243-2014

Ueno, K., Shiraiwa, T., & Yamada, T. (1993). Precipitation environment in the Langtang Valley, Nepal Himalayas. *IAHS Publication*, *218*, 207–219.

Ueno, K., & Yamada, T. (1990). Diurnal variation of precipitation in Langtang Valley, Nepal Himalayas. *Bulletin of Glacier Research*, *8*, 93–101.

Uppala, S. M., Kållberg, P. W., Simmons, A. J., Andrae, U., Bechtold, V. D. C., Fiorino, M., et al. (2005). The ERA-40 re-analysis. *Quarterly Journal of the Royal Meteorological Society*, *131*(612), 2961–3012. https://doi.org/10.1256/qj.04.176

Usha, K. H., Nair, V. S., & Babu, S. S. (2022). Effects of aerosol-induced snow albedo feedback on the seasonal snowmelt over the Himalayan region. *Water Resources Research*, *58*, e2021WR030140. https://doi.org/10.1029/2021WR030140

van Tiel, M., Stahl, K., Freudiger, D., & Seibert, J. (2020). Glacio-hydrological model calibration and evaluation. *Wiley Interdisciplinary Reviews: Water*, *7*(6), e1483–e1487.

Vionnet, V., Marsh, C. B., Menounos, B., Gascoin, S., Wayand, N. E., Shea, J., et al. (2021). Multi-scale snowdrift-permitting modelling of mountain snowpack. *The Cryosphere*, *15*(2), 743–769. https://doi.org/10.5194/tc-15-743-2021

Vionnet, V., Martin, E., Masson, V., Guyomarc'h, G., Naaim-Bouvet, F., Prokop, A., et al. (2014). Simulation of wind-induced snow transport and sublimation in alpine terrain using a fully coupled snowpack/atmosphere model. *The Cryosphere*, *8*(2), 395–415. https://doi.org/10.5194/tc-8-395-2014

Viviroli, D., Dürr, H. H., Messerli, B., Meybeck, M., & Weingartner, R. (2007). Mountains of the world, water towers for humanity: Typology, mapping, and global significance. *Water Resources Research*, *43*, W07447. https://doi.org/10.1029/2006WR005653

Vivoni, E. R., Di Benedetto, F., Grimaldi, S., & Eltahir, E. A. (2008). Hypsometric control on surface and subsurface runoff. *Water Resources Research*, *44*, W12502. https://doi.org/10.1029/2008WR006931

Wang, L. H., He, X. B., Steiner, J. F., Zhang, D. W., Wu, J. K., Wang, S. Y., & Ding, Y. J. (2020). Models and measurements of seven years of evapotranspiration on a high elevation site on the Central Tibetan Plateau. *Journal of Mountain Science*, *17*(12), 3039–3053. https://doi.org/10.1007/s11629-020-6051-1

Warrick, A. W., & Nielsen, D. R. (1980). Spatial variability of soil physical properties in the field. In D. Hillel (Ed.), *Applications of soil physics* (pp. 319–344). Academic Press.

Weidberg, N., Wethey, D. S., & Woodin, S. A. (2021). Global intercomparison of hyper-resolution ECOSTRESS coastal sea surface temperature measurements from the space station with VIIRS-N20. *Remote Sensing*, *13*(24), 5021. https://doi.org/10.3390/rs13245021

Wijngaard, R. R., Steiner, J. F., Kraaijenbrink, P. D., Klug, C., Adhikari, S., Banerjee, A., et al. (2019). Modeling the response of the Langtang Glacier and the hintereisferner to a changing climate since the little ice age. *Frontiers in Earth Science*, *7*, 143. https://doi.org/10.3389/feart.2019.00143

Wilson, A. M., Williams, M. W., Kayastha, R. B., & Raco viteanu, A. (2016). Use of a hydrologic mixing model to examine the roles of meltwater, precipitation and groundwater in the Langtang River basin, Nepal. *Annals of Glaciology*, *57*(71), 155–168. https://doi.org/10.3189/2016aog71a067

Winiger, M. G. H. Y., Gumpert, M., & Yamout, H. (2005). Karakorum-Hindukush-western Himalaya: Assessing high-altitude water resources. *Hydrological Processes: International Journal*, *19*(12), 12–2338. https://doi.org/10.1002/hyp.5887

Yang, D., Goodison, B. E., Metcalfe, J. R., Golubev, V. S., Bates, R., Pangburn, T., & Hanson, C. L. (1998). Accuracy of NWS 800 standard nonrecording precipitation gauge: Results and application of WMO intercomparison. *Journal of Atmospheric and Oceanic Technology*, *15*(1), 54–68. https://doi.org/10.1175/1520-0426(1998)015<0054:aonsnp>2.0.co;2

Yao, T., Bolch, T., Chen, D., Gao, J., Immerzeel, W., Piao, S., et al. (2022). The imbalance of the Asian water tower. *Nature Reviews Earth & Environment*, *3*(10), 618–632. https://doi.org/10.1038/s43017-022-00299-4

Yoon, Y., Kumar, S. V., Forman, B. A., Zaitchik, B. F., Kwon, Y., Qian, Y., et al. (2019). Evaluating the uncertainty of terrestrial water budget components over High Mountain Asia. *Frontiers in Earth Science*, *7*, 120. https://doi.org/10.3389/feart.2019.00120

Yuan, L., Ma, Y., Chen, X., Wang, Y., & Li, Z. (2021). An enhanced MOD16 evapotranspiration model for the Tibetan Plateau during the unfrozen season. *Journal of Geophysical Research: Atmospheres*, *126*, e2020JD032787. https://doi.org/10.1029/2020JD032787

Zhang, Y., Kong, D., Gan, R., Chiew, F. H. S., McVicar, T. R., Zhang, Q., & Yang, Y. (2019). Coupled estimation of 500m and 8-day resolution global evapotranspiration and gross primary production in 2002–2017. *Remote Sensing of Environment*, *222*, 165–182.

Zhao, M., Heinsch, F. A., Nemani, R. R., & Running, S. W. (2005). Improvements of the MODIS terrestrial gross and net primary production global data set. *Remote Sensing of Environment*, *95*(2), 164–176. https://doi.org/10.1016/j.rse.2004.12.011

References From the Supporting Information

Berthier, E., Vincent, C., Magnússon, E., Gunnlaugsson, Á. Þ., Pitte, P., Le Meur, E., et al. (2014). Glacier topography and elevation changes derived from Pléiades sub-meter stereo images. *The Cryosphere*, *8*(6), 2275–2291. https://doi.org/10.5194/tc-8-2275-2014

Cuffey, K. M., & Paterson, W. S. B. (2010). *The physics of glaciers* (4th ed.). Academic Press.

Hall, D. K., & Riggs, G. A. (2021). *MODIS/Terra snow cover daily L3 global 500m SIN grid, version 61*. NASA National Snow and Ice Data Center Distributed Active Archive Center. https://doi.org/10.5067/MODIS/MOD10A1.061

Millan, R., Mouginot, J., Rabatel, A., & Morlighem, M. (2022). Ice velocity and thickness of the world's glaciers. *Nature Geoscience*, *15*(2), 124–129. https://doi.org/10.1038/s41561-021-00885-z

Miralles, D. G., Holmes, T. R. H., de Jeu, R. A. M., Gash, J. H., Meesters, A. G. C. A., & Dolman, A. J. (2011). Global land-surface evaporation estimated from satellite-based observations. *Hydrology and Earth System Sciences*, *15*(2), 453–469. https://doi.org/10.5194/hess-15-453-2011

Myneni, R., & Knyazikhin, Y. (2018). *VIIRS/NPP leaf area index/FPAR 8-day L4 global 500m SIN grid V001*. NASA EOSDIS Land Processes DAAC. https://doi.org/10.5067/VIIRS/VNP15A2H.001

Pelletier, J. D., Broxton, P. D., Hazenberg, P., Zeng, X., Troch, P. A., Niu, G. Y., et al. (2016). A gridded global data set of soil, intact regolith, and sedimentary deposit thicknesses for regional and global land surface modeling. *Journal of Advances in Modeling Earth Systems*, *8*, 41–65. https://doi.org/10.1002/2015MS000526

Renner, M., Wild, M., Schwarz, M., & Kleidon, A. (2019). Estimating shortwave clear-sky fluxes from hourly global radiation records by quantile regression. *Earth and Space Science*, *6*, 1532–1546. https://doi.org/10.1029/2019EA000686

Shangguan, W., Hengl, T., Mendes de Jesus, J., Yuan, H., & Dai, Y. (2017). Mapping the global depth to bedrock for land surface modeling. *Journal of Advances in Modeling Earth Systems*, *9*, 65–88. https://doi.org/10.1002/2016MS000686

Sterckx, S., Benhadj, I., Duhoux, G., Livens, S., Dierckx, W., Goor, E., et al. (2014). The PROBA-V mission: Image processing and calibration. *International Journal of Remote Sensing*, *35*(7), 2565–2588. https://doi.org/10.1080/01431161.2014.883094

van Tricht, L., Huybrechts, P., Van Breedam, J., Vanhulle, A., Van Oost, K., & Zekollari, H. (2021). Estimating surface mass balance patterns from unoccupied aerial vehicle measurements in the ablation area of the Morteratsch-Pers glacier complex (Switzerland). *The Cryosphere*, *15*(9), 4445–4464. https://doi.org/10.5194/tc-15-4445-2021